

CHALMERS
UNIVERSITY OF TECHNOLOGY

Exploiting Structural Sparsity and Delay-Doppler Decoupling for Low-Complexity OTFS-ISAC Receivers

Downloaded from: https://research.chalmers.se, 2026-11-05 05:16 UTC

Citation for the original published paper (version of record):
Marchese, M., Keskin, M., Savazzi, P. et al (2026). Exploiting Structural Sparsity and Delay-Doppler Decoupling for Low-Complexity OTFS-ISAC
Receivers. IEEE Open Journal of the Communications Society, 7: 12886-12906.
http://dx.doi.org/10.1109/OJCOMS.2026.3741196

N.B. When citing this work, cite the original published paper.

© 2026 IEEE. Personal use of this material is permitted. Permission from IEEE must be obtained for all other uses, in any current or future media, including reprinting/republishing this material for advertising or promotional purposes, or reuse of any copyrighted component of this work in other works.

(article starts on next page)

Received 11 September 2026; accepted 3 October 2026. Date of publication 7 October 2026; date of current version 15 October 2026.

Digital Object Identifier 10.1109/OJCOMS.2026.3741196

Exploiting Structural Sparsity and Delay-Doppler Decoupling for Low-Complexity OTFS-ISAC Receivers

MAURO MARCHESE[1] (Graduate Student Member, IEEE), MUSA FURKAN KESKIN[2] (Senior Member, IEEE), PIETRO SAVAZZI[1,3] (Senior Member, IEEE), AND HENK WYMEERSCH[2] (Fellow, IEEE)

[1]Department of Electrical, Computer and Biomedical Engineering, University of Pavia, 27100 Pavia, Italy
[2]Department of Electrical Engineering, Chalmers University of Technology, 412 96 Gothenburg, Sweden
[3]Consorzio Nazionale Interuniversitario per le Telecomunicazioni (CNIT), 43124 Parma, Italy

CORRESPONDING AUTHOR: M. MARCHESE (mauro.marchese01@universitadipavia.it)

This work was supported in part by Vinnova FFI Project (Beyond 5GPOS) under Grant 2022-01640; in part by Swedish Research Council (VR) through the Project 6GPERCEF under Grant 2024-04390; and in part by European Union through Italian National Recovery and Resilience Plan (NRRP) of NextGenerationEU, partnership on "Telecommunications of the Future" (program "RESTART") under Grant PE00000001.

ABSTRACT In this work, the problems of channel estimation, radar sensing, and data detection are addressed for monostatic integrated sensing and communications (ISAC) applications within orthogonal time frequency space (OTFS) systems operating with a reduced cyclic prefix (RCP). Specifically, the delay-Doppler (DD) input-output relationship is formulated in a discrete representation that enables signalindependent disjoint parameter estimation by encapsulating fractional delay and Doppler effects through distinct, structurally sparse matrices. This exact algebraic separability is directly exploited to develop a low-complexity parameter estimation framework for the communication channel, which is seamlessly adapted for monostatic radar sensing on backscattered data frames. To enhance path detection robustly and safeguard estimation accuracy under low signal-to-noise ratio (SNR) regimes where traditional stopping criterion (SC)-based methods fail, a deep learning (DL) architecture is integrated to perform model order selection via multi-class classification. Furthermore, a path-wise variant of the iterative Landweber method, designated as iterative matched filtering and combining (IMFC), is introduced for low-complexity data detection by leveraging the identical structural sparsity unlocked by the decoupled framework. Simulation results indicate the proposed estimation scheme achieves lower normalized mean squared error (NMSE) than conventional channel estimation algorithms and sensing performance close to the Cramér-Rao lower bound (CRLB). Finally, the IMFC equalizer is shown to deliver bit error rate (BER) performance comparable to the traditional linear minimum mean squared error (LMMSE) benchmark while dramatically reducing the computational load.

INDEX TERMS OTFS, integrated sensing and communications (ISAC), parameter estimation, deep learning (DL), reduced-complexity equalization.

I. INTRODUCTION

HIGH-MOBILITY scenarios are becoming increasingly prevalent with the ongoing development of next-generation wireless networks [1], [2]. As such, novel waveforms have been investigated to accommodate these emerging use cases, including high-speed railways (HSR), vehicle-to-infrastructure (V2I), and vehicle-to-vehicle (V2V) communications where speeds up to 500 km/h are experienced [3]. The conventional orthogonal frequency division multiplexing (OFDM) scheme adopted in 4G/5G systems robust to intersymbol interference (ISI) becomes impractical in such conditions, as its performance degrades significantly in high-Doppler channels [4] due to intercarrier interference (ICI). orthogonal time frequency space (OTFS) is a 2D modulation scheme proposed in [3] and [5] and is considered a strong candidate waveform for 6G networks due to its resilience to high-Doppler effects in high-mobility scenarios. OTFS has been shown [3] to deliver superior performance in high-Doppler environments. Furthermore, OTFS is well-suited for sensing due to its inherent

© 2026 The Authors. This work is licensed under a Creative Commons Attribution 4.0 License.
For more information, see https://creativecommons.org/licenses/by/4.0/

delay-Doppler channel representation [6], [7]. Moreover, OTFS exhibits lower peak-to-average power ratio (PAPR) compared to OFDM [8], [9]. This encourages considering an integrated sensing and communications (ISAC) system where a dual-functional transmitter is used for both communication and sensing. While OTFS demonstrates significant potential in high-Doppler scenarios, its practical implementation hinges on the development of efficient algorithms for channel estimation and data detection. Channel estimation plays a pivotal role as the receiver's ability to decode data depends on an accurate representation of the channel. Therefore, in order to enhance the feasibility of OTFS for next-generation wireless ISAC systems, *novel low-complexity algorithms must be developed for channel estimation, radar sensing, and data detection*.

A. STATE OF THE ART

1) CHANNEL ESTIMATION

Several algorithms have been proposed in the literature for OTFS channel estimation. In [10] and [11], a threshold method was proposed, achieving good performance in both integer delays-Dopplers (DDs) and fractional Doppler scenarios. Channel sparsity is exploited in [12] to design an orthogonal matching pursuit (OMP) algorithm for OTFS channel estimation. sparse Bayesian learning (SBL) algorithms for channel estimation have also been explored in [13], [14], [15], and [16]. Low-complexity channel estimation schemes, enabling disjoint delay-Doppler estimation in fractional DDs scenarios, are proposed in [17], [18], and [19]. Specifically, the low-complexity disjoint delay-Doppler estimation schemes in [17] and [18] achieve decoupling by strictly relying on the transmission of an isolated impulse pilot with an appropriately sized guard zone. In such frameworks, the delay-Doppler separability is a signal-dependent property observed at the receiver side, which vanishes when arbitrary data symbols are transmitted as usual in ISAC systems. In more detail, in [17] and [18], an approximate maximum likelihood (ML) estimation algorithm, derived under the assumption of large OTFS frame size, is proposed. In fact, if this condition holds, multipaths are well separated in the delay-Doppler (DD) domain and the columns of the constituent delay-Doppler parameter matrix (CDDPM) [20], [21] become orthogonal [17], [18]. Under the assumption of good separability of received pilot replicas due to fine delay and Doppler resolutions, the algorithms in [17] and [18] outperform the methods in [10] and [12] and SBL methods. When delay and Doppler resolutions are not fine enough, received pilot replicas spread into adjacent DD bins, causing non-negligible interpath interference (IPI) that limits estimation accuracy. To this end, channel estimation in high-IPI scenarios has been addressed in [20] and [21]. In [20], a delay-Doppler interpath interference cancellation (DDIPIC) algorithm is proposed, employing refinement procedures to cancel IPI. This approach outperforms the method from [17], at the cost of higher complexity. Conversely, in [21], a variant of the DDIPIC algorithm, called progressive interpath interference cancellation (PIPIC), is introduced to reduce complexity and enhance estimation accuracy. It is shown that a single global refinement step is sufficient to achieve high estimation accuracy and suppress IPI, surpassing the performance of DDIPIC. However, despite their resilience in high-IPI scenarios, the algorithms in [20] and [21] perform joint DD estimation.

Nevertheless, the methodologies proposed in [17], [18], [20], and [21] are based on a DD input/output relation that accounts for fractional channel parameters and is quite complicated since it stems from continuous-time analysis [7], [17], [18]. A more compact expression for the DD input-output (I/O) relation in matrix form is provided in [22]. This expression is valid for OTFS with a single cyclic prefix (CP) (referred to in the literature as reduced cyclic prefix (RCP)-OTFS [11], [22]) and assumes integer delays and Doppler shifts. A compact DD I/O relation accounting for fractional DDs has been derived in [23]. However, the relation between the expression proposed in [23] has not been related to the well-known integer DD based expression from [22]. Moreover, in [23], a joint DD estimation algorithm has been developed for fractional DD channels. Finally, the approaches in [17], [18], [19], [20], [21], and [24] use stopping criteria to detect multiple paths. This may lead to poor estimation performance at low signal-to-noise ratio (SNR) where small amplitude paths may be missed.

Since deep learning (DL) has emerged as a powerful tool for channel estimation, offering reduced computational cost and latency while improving accuracy, several DL-based approaches have been proposed in the OTFS literature to enhance channel state information extraction [25], [26], [27], improve robustness to noise [28], [29], refine model-based estimates [30], and reduce computational complexity [24], [31].

2) RADAR SENSING

As OTFS exhibits good properties for sensing [9], [32], several approaches have been investigated. In [20], the DDIPIC algorithm is shown to achieve good sensing performance in an ISAC context in which the transmitter estimates the radar parameters of the target receiver. Although in [20] a single-target scenario has been considered, the DDIPIC algorithm can be used for multi-target detection and parameter estimation. Other radar sensing algorithms in single-antenna systems are considered in [33] and [34], where matched filter (MF) radar and generalized likelihood ratio test (GLRT) based algorithms are proposed, respectively. In [34], ISI and ICI effects are exploited to overcome the ambiguity barrier of conventional sensing algorithms in OTFS systems. OTFS-based ISAC in multiple input multiple output (MIMO) systems has been considered in [35], [36], [37], and [38]. However, such approaches entail joint DD estimation of radar target parameters [20], [34], [35], [36], [37], thereby

compounding the computational burden through a multi-dimensional search space.

3) DATA DETECTION

Various approaches have been investigated to reduce complexity and enhance detection performance. Similar to OFDM, simple single-tap equalization is considered in [11], but its performance is acceptable only in quasi-static (very low-mobility) multipath channels. For high-mobility scenarios, the traditional linear minimum mean squared error (LMMSE) estimator [11] can be employed to achieve better performance. In [39], [40], [41], and [42], various LMMSE detector variants have been proposed to mitigate the high computational complexity caused by the matrix inversion required in LMMSE, while maintaining good detection performance. However, biorthogonality [39] and integer channel parameters [40] are assumed. A more efficient approach exploiting sparsity in the DD domain is presented in [11] and [43], where detection is formulated over a sparsely connected factor graph and solved via the message passing (MP) algorithm. However, the computational advantage of MP relies strictly on the high sparsity of the DD channel matrix, which holds only under ideal integer DD assumptions. In practical scenarios with fractional DD shifts, energy leakage across adjacent delay-Doppler bins causes the channel matrix to become significantly denser. As a result, the factor graph expands massively into a densely connected topology, causing the computational complexity of the iterative message updates to explode and rendering the practical implementation of MP-based detection virtually infeasible.

B. CONTRIBUTIONS

In this work, the problem of channel estimation, radar sensing and data detection in RCP-OTFS systems with fractional DDs is investigated. Given the above description of the existing OTFS literature, the following points are addressed in this paper: *(i)* formulation of a compact expression for the DD channel matrix accounting for fractional channel parameters and enabling signal-independent separate DD estimation, whereas conventional disjoint DD estimation algorithms strictly rely on an impulse-pilot-based assumption [17], [18]; *(ii)* enhancing path detection and channel estimation accuracy at low SNR values, where conventional stopping criterion (SC)-based approaches miss small amplitude paths; *(iii)* design of a reduced-complexity equalization algorithm for fractional DD case that relies on the intrinsic properties of DD parameter matrices by relaxing the assumptions made in [39] and [40]. Thus, the contributions of this work are as follows:

- **Signal-independent algebraic delay-Doppler separability framework:** Unlike existing disjoint fractional DD estimation methods [17], [18] that rely on continuous-time formulations, asymptotic approximations valid only for large frame sizes, and signal-dependent parameter matrices embedded with a impulse pilot signal, a rigorous, closed-form algebraic decomposition of the RCP-OTFS channel matrix is developed. It is demonstrated that fractional delay and Doppler effects can be rigorously decoupled into distinct, structurally sparse parameter matrices. This separability is completely independent of the transmitted signal, ensuring that DD decoupling and structural sparsity can be exploited also in data-based ISAC (i.e., when random data symbols are transmitted). Leveraging this separability, a correlation-based parameter estimation algorithm is proposed for OTFS-ISAC, which reduces the multi-dimensional search over the DD domain into two independent, one-dimensional optimization problems.
- **Enhanced model order selection at low SNR via DL**: As conventional channel estimation algorithms rely on a SC to detect multiple paths, performance heavily depends on the choice of the convergence tolerance parameter for the SC, and at low SNR, multiple paths are often missed. To enhance detection capabilities and estimation accuracy at low SNR, a DL architecture is introduced to estimate the number of propagation paths by formulating the estimation problem as a multi-class classification task.
- **Reduced-complexity Landweber method for channel equalization**: A path-wise version of the Landweber method, exploiting sparsity of DD parameter matrices and exact DD separability, is proposed for data detection to reduce the equalization complexity against the LMMSE estimator. This algorithm, called iterative matched filtering and combining (IMFC), iteratively combines the outputs of matched filters (MFs) parametrized by different delays/Dopplers to estimate data symbols. This approach offers significantly lower complexity than the traditional LMMSE estimator while achieving nearly the same bit error rate (BER) performance.

Importantly, the above contributions are not developed as independent processing blocks, but originate from a unified structure-exploiting OTFS-ISAC framework. The proposed algebraic decomposition of the fractional DD RCP-OTFS channel into path-wise components provides the core structure exploited throughout the receiver. First, its delay-Doppler separability enables low-complexity disjoint parameter estimation, complemented by the feedforward neural network (FNN)-based model-order selection, and is directly employed for radar sensing on backscattered frames. Finally, once parameters are estimated, the same path-wise decomposition and structural sparsity are reused for communication data detection via the proposed IMFC equalizer.

Notation: The superscripts $(\cdot)^*$, $(\cdot)^\top$, and $(\cdot)^{\mathsf{H}}$ denote element-wise complex conjugation, transpose, and Hermitian transpose, respectively. $\|\mathbf{X}\|_F$, represents the Frobenius norm. $\mathbf{I}_N$ is the identity matrix of order N. The operators $\mathrm{vec}(\mathbf{X})$ and $\mathrm{vec}^{-1}_{M,N}(\mathbf{x})$ represent the vectorization of matrix $\mathbf{X}$ and the reshaping of vector $\mathbf{x}$ back into a $M \times N$ matrix, respectively. $\otimes$, $\odot$ and $\times$ represent the Kronecker (tensor), Hadamard

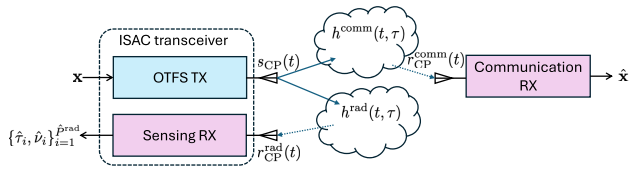


FIGURE 1. The RCP-OTFS ISAC system including: a dual-functional ISAC transceiver for data communication and radar sensing (OTFS TX and Sensing RX are mounted on the same hardware) and a communication receiver.

(element-wise) and Cartesian products, respectively. Finally, $\rho(\cdot)$ denotes the spectral radius, which is the maximum absolute eigenvalue of the argument, and $[\cdot]_A$ denotes the modulo-A operation.

II. RCP-OTFS SYSTEM MODEL

The considered ISAC scenario includes a dual-functional OTFS transceiver (made of a single-antenna transmitter for communication and a radar sensing receiver mounted on the same hardware platform) and a single-antenna communication receiver, as shown in Fig. 1. In this scenario, it is assumed that there exists a geometric coherence time during which the channel parameters (channel gains, delays and Doppler shifts) can be considered constant [11]. Typically, these geometric coherence intervals of the DD channel are significantly longer than the transmission duration of individual OTFS frames [11]. Specifically, while the complex path gains inherently undergo deterministic phase rotations from one frame to the next due to mobility, they can be treated as invariant across consecutive frames modulo this phase shift, which is known a priori and easily compensated for once the Doppler shifts are estimated. Therefore, in order to avoid interference between pilot and data symbols due to fractional delays and Dopplers, the transmitter sends, within this geometric coherence window, a single pilot frame for channel estimation, followed by a sequence of data frames [17], [20], [21], [24], [31]. It is worth noting that while conventional embedded pilot-aided strategies are widely used for integer channels, they become highly inefficient in fractional delay-Doppler regimes [11]. Under an embedded setup, mitigating the resulting severe interference would mandate an excessively large guard zone around the pilot impulse, thereby drastically increasing the transmission overhead and undermining the spectral efficiency [11]. Conversely, the considered separate pilot-and-data frame strategy entirely bypasses data-to-pilot interference without incurring prohibitive overhead penalties, taking full advantage of the long geometric coherence time of the DD channel. A numerical assessment that justifies the considered separate pilot and data frames is provided in Section VI-A, where the frame duration is compared with the typical geometric coherence intervals of the DD channel.

At the receiver side, the communication receiver processes the pilot frame for estimating the communication channel. Afterwards, it uses the channel estimate to detect incoming data frames. In the meanwhile, the transmit signal is reflected off multiple targets in the environment. The backscattered data frames are used by the sensing receiver to estimate range and velocity of the targets [20].

A. TRANSMIT SIGNAL MODEL

The OTFS system is characterized by M subcarriers and N time slots. The subcarrier spacing is $\Delta f = 1/T$, where T represents the OTFS block duration. Therefore, the signal bandwidth is $M\Delta f$, and the overall frame duration is NT. The OTFS modulator arranges MN information symbols in the DD domain over the two-dimensional grid $I_{DD} = \{m\Delta\tau, n\Delta\nu \mid 0 \le m \le M-1,\ 0 \le n \le N-1\}$, where $\Delta\tau = 1/(M\Delta f)$ and $\Delta\nu = 1/(NT)$ represent the delay and Doppler resolutions, respectively. Hence, the DD matrix $\mathbf{X} \in \mathbb{C}^{M\times N}$ is obtained. The information symbols are selected from an alphabet with Q constellation points. The n-th OTFS symbol is given by the Heisenberg transform as

$$s_n(t) = \sum_{m=0}^{M-1} \left[\mathbf{X}_{\mathrm{tf}}\right]_{m,n} e^{j2\pi m\Delta f t} g_{\mathrm{tx}}(t), \quad 0 < t < T, \tag{1}$$

where $g_{\mathrm{tx}}(t)$ is the transmit pulse shaping waveform, and $\mathbf{X}_{\mathrm{tf}} \in \mathbb{C}^{M\times N}$ is the time-frequency samples matrix. The delay-Doppler symbols are converted to time-frequency samples using the inverse symplectic finite Fourier transform (ISFFT) as $\mathbf{X}_{\mathrm{tf}} = \mathbf{F}_M \mathbf{X} \mathbf{F}_N^{\mathsf{H}}$ where $[\mathbf{F}_N]_{p,q} = \frac{1}{\sqrt{N}} e^{-j2\pi \frac{pq}{N}}$ is the N-point unitary discrete Fourier transform (DFT) matrix. The entire time-domain OTFS signal is then given by

$$s(t) = \sum_{n=0}^{N-1} s_n(t - nT). \tag{2}$$

In RCP-OTFS [11], [22] systems the overall transmitted signal is preceded by a single cyclic prefix of duration T_{CP}. Hence, the transmitted RCP-OTFS signal is given as

$$s_{\mathrm{CP}}(t) = \begin{cases} s(t), & 0 \le t \le NT \\ s(t+NT), & -T_{\mathrm{CP}} \le t \le 0 \end{cases}. \tag{3}$$

The duration of the CP is chosen such that $T_{\mathrm{CP}} \ge \sigma_\tau$, where σ_τ is the channel delay spread. Sampling (1) at $t = qT/M$ with $q = 0, 1, \ldots, M-1$ and stacking samples into a vector, (1) can be expressed in matrix form as

$$\mathbf{s}_n = \mathbf{G}_{\mathrm{tx}} \mathbf{F}_M^{\mathsf{H}} \left[\mathbf{X}_{\mathrm{tf}}\right]_{:,n} \tag{4}$$

where $\mathbf{G}_{\mathrm{tx}} = \mathrm{diag}\left\{g_{\mathrm{tx}}(0), g_{\mathrm{tx}}\left(\frac{T}{M}\right), \ldots, g_{\mathrm{tx}}\left(\frac{(M-1)T}{M}\right)\right\}$. The overall transmit samples are then obtained as

$$\mathbf{S} = [\mathbf{s}_1\ \mathbf{s}_2\ \ldots\ \mathbf{s}_N] = \mathbf{G}_{\mathrm{tx}} \mathbf{F}_M^{\mathsf{H}} \mathbf{X}_{\mathrm{tf}} = \mathbf{G}_{\mathrm{tx}} \mathbf{X} \mathbf{F}_N^{\mathsf{H}}. \tag{5}$$

By vectorizing (5), the transmit samples vector is given by

$$\mathbf{s} = \mathrm{vec}(\mathbf{S}) = \left(\mathbf{F}_N^{\mathsf{H}} \otimes \mathbf{G}_{\mathrm{tx}}\right) \mathrm{vec}(\mathbf{X}) = \left(\mathbf{F}_N^{\mathsf{H}} \otimes \mathbf{G}_{\mathrm{tx}}\right) \mathbf{x}. \tag{6}$$

In case of rectangular pulse shaping $\mathbf{G}_{\mathrm{tx}} = \mathbf{I}_M$, thus (6) reduces to the well-known inverse discrete Zak transform (IDZT) [11]. Hereafter, OTFS with rectangular pulse shaping is considered as it outperforms other pulse shaping waveforms [22].

B. HIGH-MOBILITY COMMUNICATION AND RADAR CHANNEL

The high-mobility communication and radar channel is made of a certain number of mobile scatterers. Therefore, the delay-time impulse response of the channel with P resolvable paths can be obtained as[1]

$$h(t,\tau) = \sum_{i=1}^{P} g_i e^{j2\pi\nu_i t}\delta(\tau-\tau_i), \tag{7}$$

where g_i, τ_i and ν_i are the complex channel gain, the propagation delay and the Doppler shift of the i-th reflected path, respectively. For radar sensing, $\tau_i = \frac{2d_i}{c}$ is the round trip delay (RTD) where d_i is the target range and c is the speed of light; and $\nu_i = \frac{2v}{c} f_c$ where v is the radial velocity of the target and f_c is the carrier frequency.

C. RECEIVED SIGNAL MODEL

The received signal at both communication and sensing receivers is expressed as

$$\begin{aligned} r_{\mathrm{CP}}(t) &= \int h(t,\tau)s_{\mathrm{CP}}(t-\tau)\mathrm{d}\tau + n(t) \\ &= \sum_{i=1}^{P} g_i s_{\mathrm{CP}}(t-\tau_i)e^{j2\pi\nu_i t} + n(t), \end{aligned} \tag{8}$$

where $n(t)$ is additive white Gaussian noise (AWGN) with monolateral power spectral density (PSD) N_0.

III. NOVEL RCP-OTFS ISAC MODEL FORMULATION

A. TIME DOMAIN ANALYSIS FOR RCP WAVEFORMS

In this section, the expression for the delay-time channel matrix is derived. Let's consider a multicarrier RCP waveform with MN symbols per frame. The received signal is obtained according to (8). The received signal without CP is given as [22], [34], [37]

$$r(t) = \sum_{i=1}^{P} g_i s([t-\tau_i]_{NT})e^{j2\pi\nu_i t} + n(t). \tag{9}$$

By sampling at the symbol rate, the following discrete observations, expressed in matrix form, are obtained

$$\mathbf{r} = \mathbf{H}\mathbf{s} + \mathbf{n}, \tag{10}$$

where $\mathbf{H} \in \mathbb{C}^{MN\times MN}$ is the delay-time channel matrix and $\mathbf{n} \sim \mathcal{CN}(\mathbf{0}, \sigma^2\mathbf{I}_{MN}) \in \mathbb{C}^{MN\times 1}$ is the AWGN vector.

Theorem 1: Given the I/O relation in (10), the delay-time channel matrix is given by

$$\mathbf{H} = \sum_{i=1}^{P} g_i \mathbf{D}^{K_i}\mathbf{D}^{\tilde{k}_i}\mathbf{F}_{MN}^{\mathsf{H}}(\mathbf{D}^*)^{L_i}(\mathbf{D}^*)^{\tilde{l}_i}\mathbf{F}_{MN}, \tag{11}$$

where $\mathbf{D} = \mathrm{diag}\{[z^q]_{q=0}^{MN-1}\}$ with $z = e^{j\frac{2\pi}{MN}}$, $L_i = \mathrm{round}\left(\frac{\tau_i}{\Delta\tau}\right)$ denotes the integer delay, $\tilde{l}_i = \frac{\tau_i - L_i\Delta\tau}{\Delta\tau}$ denotes the fractional delay, $K_i = \mathrm{round}\left(\frac{\nu_i}{\Delta\nu}\right)$ denotes the integer Doppler and $\tilde{k}_i = \frac{\nu_i - K_i\Delta\nu}{\Delta\nu}$ denotes the fractional Doppler.

Proof: See Appendix A. ∎

Theorem 1 generalizes the results in [22] by removing the simplifying assumption of integer channel parameters. It can be noted that a similar expression of the delay-time channel matrix accounting for fractional channel parameters has been proposed in [23], without investigating DD decoupling.

Corollary 1: If channel parameters assume integer values ($\tilde{l}_i = 0, \tilde{k}_i = 0$), then the delay-time channel matrix reduces to

$$\mathbf{H} = \sum_{i=1}^{P} g_i \mathbf{D}^{K_i}\mathbf{\Pi}^{L_i}, \tag{12}$$

where $\Pi = [\mathbf{e}_2\ \mathbf{e}_3\ \ldots\ \mathbf{e}_{MN}\ \mathbf{e}_1]$ is the forward cyclic shift permutation matrix and $\mathbf{e}_i$ is a one-hot vector defined as $[\mathbf{e}_i]_q = \delta_{iq}$.

Proof: See Appendix B. ∎

From Corollary 1, it is evident that the derived expression for the delay-time channel matrix in (11) serves as a generalization of (12) presented in [22]. Furthermore, it can be observed that the effects of propagation delays and Doppler shifts are encapsulated through the same diagonal matrix $\mathbf{D}$.

B.: NOVEL FORMULATION OF THE DELAY-DOPPLER ISAC MODEL

In this section, a novel formulation of the DD expression for the ISAC channel, enabling disjoint DD estimation, is derived based on the result presented in Theorem 1.

Given the received samples vector $\mathbf{r}$ from (10), the information symbol vector is obtained by inverting (6) as [11], [22]

$$\mathbf{y} = \left(\mathbf{F}_N \otimes \mathbf{I}_M\right)\mathbf{r}. \tag{13}$$

As shown in [11] and [22], combining (6), (10) and (13) the I/O relation in the DD domain can be written as

$$\mathbf{y} = \mathbf{H}_{\mathrm{DD}}\mathbf{x} + \mathbf{w}, \tag{14}$$

where $\mathbf{w} = \left(\mathbf{F}_N \otimes \mathbf{I}_M\right)\mathbf{n}$ is the AWGN noise vector in the DD domain and

$$\mathbf{H}_{\mathrm{DD}} = \left(\mathbf{F}_N \otimes \mathbf{I}_M\right)\mathbf{H}\left(\mathbf{F}_N^{\mathsf{H}} \otimes \mathbf{I}_M\right), \tag{15}$$

is the DD channel matrix. It can be noticed that $\mathbf{w}$ is zero mean with covariance matrix

$$\begin{aligned} \mathbf{C}_{\mathrm{w}} &= \mathbb{E}\left[\mathbf{w}\mathbf{w}^{\mathsf{H}}\right] = \left(\mathbf{F}_N \otimes \mathbf{I}_M\right)\mathbb{E}\left[\mathbf{n}\mathbf{n}^{\mathsf{H}}\right]\left(\mathbf{F}_N^{\mathsf{H}} \otimes \mathbf{I}_M\right) \\ &= \sigma^2\left(\mathbf{F}_N\mathbf{F}_N^{\mathsf{H}} \otimes \mathbf{I}_M^2\right) = \sigma^2\left(\mathbf{I}_N \otimes \mathbf{I}_M\right) = \sigma^2\mathbf{I}_{MN}. \end{aligned} \tag{16}$$

Replacing (11) in (15), the DD channel matrix becomes

$$\mathbf{H}_{\mathrm{DD}} = \sum_{i=1}^{P} g_i\left(\mathbf{F}_N \otimes \mathbf{I}_M\right)\mathbf{D}^{k_i}\mathbf{F}_{MN}^{\mathsf{H}}(\mathbf{D}^*)^{l_i}\mathbf{F}_{MN}\left(\mathbf{F}_N^{\mathsf{H}} \otimes \mathbf{I}_M\right), \tag{17}$$

where $l_i = \tau_i/\Delta\tau = L_i + \tilde{l}_i$ and $k_i = \nu_i/\Delta\nu = K_i + \tilde{k}_i$ are the normalized DDs. Thus, by defining

$$\mathbf{T}_i = \left(\mathbf{F}_N \otimes \mathbf{I}_M\right)\mathbf{D}^{k_i}\mathbf{F}_{MN}^{\mathsf{H}}(\mathbf{D}^*)^{l_i}\mathbf{F}_{MN}\left(\mathbf{F}_N^{\mathsf{H}} \otimes \mathbf{I}_M\right), \tag{18}$$

[1]Here it is assumed that the time-bandwidth product is low such that Doppler-induced time-scaling effects can be neglected [37] (i.e., $s(t-\tau(t)) \approx s(t-\tau)$, where $\tau(t) = \tau - \nu t/f_c$ is the Doppler-induced time-varying delay). Conversely, frequency-domain shifts caused by the Doppler effect, which manifest as time-varying phase rotations in the time domain, cannot be neglected, leading to the channel model in (7).

the DD channel matrix is given as

$$\mathbf{H}_{\mathrm{DD}} = \sum_{i=1}^{P} g_i \mathbf{T}_i. \tag{19}$$

Moreover, it is possible to define the following matrix

$$\mathbf{Q}(a) = \left(\mathbf{F}_N \otimes \mathbf{I}_M\right)\mathbf{D}^a \mathbf{F}_{MN}^{\mathsf{H}} \left(\mathbf{F}_N \otimes \mathbf{I}_M\right) \in \mathbb{C}^{MN \times MN}, \tag{20}$$

such that

$$\mathbf{T}_i = \mathbf{Q}(k_i)\mathbf{Q}^*(l_i). \tag{21}$$

Remark 1: The effects of the propagation delay and the Doppler shift are separable since it can be observed that the matrix $\mathbf{T}_i$ in (21) is the product of a Doppler term $\mathbf{Q}(k_i)$ and a delay term $\mathbf{Q}^*(l_i)$. This notable property of the formulation in (21) enables the separate estimation of DD parameters. As a result, disjoint estimation can be performed to reduce computational complexity, avoiding a joint bidimensional search over the DD domain. Moreover, unlike previous literature where the delay and Doppler terms are decoupled within a measurement matrix [17], [18] (i.e., the CDDPM matrix [20]) that embeds the pilot signal itself, the algebraic decomposition in (21) operates directly on the channel matrix $\mathbf{H}_{\mathrm{DD}}$. Consequently, this matrix factorization holds true irrespective of the nature of the input vector $\mathbf{x}$. This fundamental generalization ensures that separability can be leveraged also when data are transmitted, thereby unlocking disjoint estimation in data-based ISAC applications.

The disjoint parameter estimation is further discussed in Section IV.

In conclusion, the following unified ISAC model for RCP-OTFS systems is obtained[2]

$$\mathbf{y} = \sum_{i=1}^{P} g_i \mathbf{Q}(k_i)\mathbf{Q}^*(l_i)\mathbf{x} + \mathbf{w}. \tag{22}$$

This model exhibits some interesting properties highlighted in the following proposition.

Proposition 1: The expression for a generic element of $\mathbf{Q}(a)$ is given by

$$\left[\mathbf{Q}(a)\right]_{p,q} = \frac{1}{N\sqrt{MN}} \sum_{k_1=0}^{N-1} e^{-j\frac{2\pi\lfloor p/M \rfloor k_1}{N}} \sum_{k_2=0}^{N-1} e^{-j\frac{2\pi k_2 \lfloor q/M \rfloor}{N}} e^{j\frac{2\pi(k_1 M + \mathrm{mod}(p,M))(a+k_2 M + \mathrm{mod}(q,M))}{MN}}. \tag{23}$$

Moreover, if M is an integer multiple of N (typical in OTFS system design), the number of non-zero elements in each row is M and the positions of that elements are $q = M\mathrm{mod}(p, N) + m$ where $m = 0, 1, \ldots, M-1$.

Proof: See Appendix C. ∎

[2]The algebraic input-output relations in (11) and (21) specifically rely on the cyclic property enabled by the RCP scheme. Other OTFS frame variants, such as zero-padding (ZP-OTFS) or reduced zero-padding (RZP-OTFS), feature non-cyclic frame structures that yield different input-output relations compared to the one in (22).

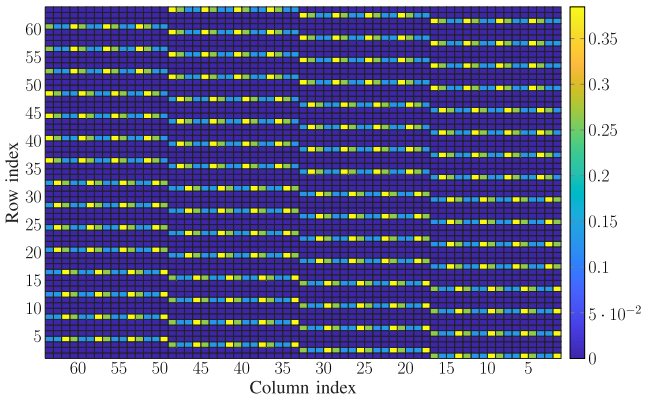


FIGURE 2. The magnitude of the elements of Q(*a*) for $M = 16$, $N = 4$ and $a = 4.4$.

Remark 2: Proposition 1 reveals the sparse structure of the $\mathbf{Q}(a)$ matrix in the proposed DD channel model in (22). In particular, it can be noted that the computation of each element of $\mathbf{Q}(a)$ has complexity $\mathcal{O}(N^2)$. Thus, the overall complexity for the computation of $\mathbf{Q}(a)$ is $\mathcal{O}(M^2N^3)$. This property is then exploited in Section IV for designing a low-complexity channel parameter estimation algorithm. It is important to mention that this sparsity stems only from the definition of the $\mathbf{Q}(a)$ matrix in (20) and does not intertwine with that of the DD channel matrix in (15), which arises from the nature of wireless channel in the DD domain [3], [11]. Furthermore, the sparsity of the DD channel matrix depends on the quantization resolution along the delay and Doppler axes [44]; consequently, it cannot be exploited in the same manner as the structural sparsity of the $\mathbf{Q}(a)$ matrix.

The structure of the $\mathbf{Q}(a)$ matrix is shown in Figure 2, where it can be noted that, with a fractional value of a, there are only M nonzero elements per row.

IV. CHANNEL ESTIMATION AND RADAR SENSING

In this section, a novel channel estimation and radar sensing algorithm is developed by leveraging the unitary and the sparsity properties of $\mathbf{Q}(a)$. The goal of channel estimation is to determine the channel parameters (P, g_i, τ_i, ν_i) by processing the received pilot signal. In this section, the pilot signal model is introduced and the proposed channel estimation algorithm is presented conditional on knowledge of P. Subsequently, the estimation of P is discussed and the proposed technique is extended for radar sensing at the ISAC transceiver.

A. PILOT SIGNAL MODEL FOR CHANNEL ESTIMATION AT COMMUNICATION RECEIVER

The single-antenna transmitter sends a pilot symbol for channel estimation in the DD domain. The DD pilot frame is given by [17], [20], [21], [24], [31]

$$[\mathbf{X}_p]_{m,n} = \begin{cases} \sqrt{E_p} & m = m_p,\ n = n_p \\ 0 & \text{otherwise} \end{cases}, \tag{24}$$

where (m_p, n_p) is the delay-Doppler resource element (DDRE) in which the pilot is sent and E_p is the energy of the transmitted pilot signal. After transmission, assuming that

the channel gains are normalized such that $\sum_{i=1}^{P} |g_i|^2 = 1$, the received pilot signal power is equal to the transmitted pilot signal power [17], [21]. The pilot signal power is defined as the pilot energy divided by the frame duration, resulting in E_p/NT. On the other hand, the noise power is calculated as the product of the noise spectral density N_0 and the signal bandwidth $M\Delta f$. Consequently, the pilot signal-to-noise ratio is expressed as:

$$\mathrm{SNR}_p = \frac{E_p}{MNN_0}. \tag{25}$$

Equivalently, $\mathrm{SNR}_p = E_p/\mathrm{tr}(\mathbf{C}_\mathrm{w}) = E_p/MN\sigma^2$. Thus, the noise variance is $\sigma^2 = N_0$.

B. PROPOSED CORRELATION-BASED CHANNEL ESTIMATION METHOD CONDITIONAL ON KNOWLEDGE OF P

As previously discussed, a low-complexity channel estimation algorithm can be developed by leveraging the sparsity of the $\mathbf{Q}(a)$ matrix through the correlation of the pilot via a bank of MFs. Furthermore, disjoint DD estimation can be performed due to the separability property highlighted in Remark 1. This allows the two-dimensional search over DD domain to be reduced to two one-dimensional search along delay and Doppler. For the time being, we assume the number of propagation paths, P, is known.

The channel parameters of multiple paths can be estimated as follows:

1) *DD initialization*: The integer part of the channel parameters can be easily obtained by identifying the maximum pilot energy in the received frame. The search space is constrained to $\mathcal{S} = [0,\ L_{\max}] \times [-K_{\max},\ K_{\max}]$. Thus, the following estimates are obtained

$$\hat{L}_i, \hat{K}_i = \arg \max_{(L,K)\in\mathcal{S}} \left| [\mathbf{Y}^{(i-1)}]_{m_p+L,n_p+K} \right|^2, \tag{26}$$

where $\mathbf{Y}^{(i-1)} = \mathrm{vec}^{-1}_{M,N}(\mathbf{y}^{(i-1)})$. In the first iteration, $\mathbf{y}^{(0)} = \mathbf{y}$.

2) *Doppler refinement*: Once the integer part is estimated, the delay is fixed at $\hat{L}_i$, while the Doppler is refined by estimating the fractional part. Specifically, the observation is passed through a filterbank of DDs parameterized by different Dopplers within the error range. Then, a MF parameterized by the fixed delay is applied. In this manner, the DD pilot is reconstructed as $\mathbf{Q}^\top(\hat{L}_i)\mathbf{Q}^\mathsf{H}(\hat{K}_i + \tilde{k})\mathbf{y}^{(i-1)}$ for different values of $\tilde{k} \in \left[-\frac{1}{2}, \frac{1}{2}\right]$. The estimate for the fractional Doppler is obtained by maximizing the magnitude of the correlation between the pilot $\mathbf{x}_p$ and the reconstructed pilot. Specifically,

$$\hat{\tilde{k}}_i = \arg \max_{\tilde{k}\in\left[-\frac{1}{2},\frac{1}{2}\right]} \left| \mathbf{x}_p^\mathsf{H}\mathbf{Q}^\top(\hat{L}_i)\mathbf{Q}^\mathsf{H}(\hat{K}_i + \tilde{k})\mathbf{y}^{(i-1)} \right|. \tag{27}$$

This refinement can be performed hierarchically to further improve accuracy by quantizing the error range in each iteration. By following this procedure for L_h iterations, the estimation error can be progressively reduced. Specifically, during the h-th iteration, the new estimate is obtained as

$$\hat{\tilde{k}}_i^{(h)} = \hat{\tilde{k}}_i^{(h-1)} + \Delta k^{(h)} \arg \max_{\kappa} \left| \mathbf{x}_p^\mathsf{H}\mathbf{Q}^\top\left(\hat{L}_i\right)\mathbf{Q}^\mathsf{H}\left(\hat{K}_i + \kappa\Delta k^{(h)}\right)\mathbf{y}^{(i-1)} \right|, \tag{28}$$

where the number of grid points is $2N_k + 1$ and $\kappa \in [-N_k, N_k]$. During the h-th iteration the resolution is $\Delta k^{(h)} = 1/(2N_k)^h$. Finally, the estimate $\hat{k}_i = \hat{K}_i + \hat{\tilde{k}}_i$ is obtained.

3) *Matched filtering*: Once the Doppler is refined, a Doppler-compensated version of the observation is obtained by passing $\mathbf{y}^{(i-1)}$ through a MF parametrized by the refined Doppler. Thus,

$$\mathbf{y}_d^{(i-1)} = \mathbf{Q}^\mathsf{H}(\hat{k}_i)\mathbf{y}^{(i-1)}. \tag{29}$$

4) *Delay refinement*: The delay is refined by estimating the fractional part. Specifically, the Doppler-compensated observation $\mathbf{y}_d^{(i-1)}$ is passed through a filterbank of MFs, each parametrized by different delays spanning the error range. The reconstructed DD pilot is then given by $\mathbf{Q}^\top(\hat{L}_i + \tilde{l})\mathbf{y}_d^{(i-1)}$ for different values of $\tilde{l} \in \left[-\frac{1}{2}, \frac{1}{2}\right]$. The estimate for the fractional delay is obtained by maximizing the magnitude of the correlation between the pilot $\mathbf{x}_p$ and the reconstructed pilot. Thus,

$$\hat{\tilde{l}}_i = \arg \max_{\tilde{l}\in\left(-\frac{1}{2},\frac{1}{2}\right)} \left| \mathbf{x}_p^\mathsf{H}\mathbf{Q}^\top(\hat{L}_i + \tilde{l})\mathbf{y}_d^{(i-1)} \right|. \tag{30}$$

Similarly to the Doppler case, the delay can be refined hierarchically for L_h times. During the h-th iteration the new estimate is obtained as

$$\hat{\tilde{l}}_i^{(h)} = \hat{\tilde{l}}_i^{(h-1)} + \Delta l^{(h)} \arg \max_{\ell} \left| \mathbf{x}_p^\mathsf{H}\mathbf{Q}^\top(\hat{L}_i + \ell\Delta l^{(h)})\mathbf{y}_d^{(i-1)} \right|, \tag{31}$$

where the number of grid points is $2N_l + 1$ and $\ell \in [-N_l, N_l]$ if $\hat{\tilde{l}}_i^{(h-1)} \neq 0$, otherwise the number of grid points is $N_l + 1$ and $\ell \in [0, N_l]$. During the h-th iteration the resolution is $\Delta l^{(h)} = 1/(2N_l)^h$. Finally, the estimate $\hat{l}_i = \hat{L}_i + \hat{\tilde{l}}_i$ is obtained.

5) *Gain estimate*: Once the DD parameters of the path are obtained $\left(\hat{\mathbf{T}}_i = \mathbf{Q}(\hat{k}_i)\mathbf{Q}^*(\hat{l}_i)\right)$, a low-complexity estimate of the channel gain can be derived by solving (22) for g_i in the noiseless single-path case. Thus, the channel gain estimate is given as the orthogonal projection of $\mathbf{y}^{(i-1)}$ onto $\hat{\mathbf{T}}_i\mathbf{x}_p$. Thus,

$$\hat{g}_i = \frac{(\hat{\mathbf{T}}_i\mathbf{x}_p)^\mathsf{H}\mathbf{y}^{(i-1)}}{\|\mathbf{x}_p\|^2} = \frac{(\hat{\mathbf{T}}_i\mathbf{x}_p)^\mathsf{H}\mathbf{y}^{(i-1)}}{E_p}. \tag{32}$$

6) *IPI cancellation*: In the multipath scenario, the channel parameters of the different paths are estimated by iterating through the previous steps P times. At the end of each iteration, a residual DD pilot vector is obtained as

$$\mathbf{y}^{(i)} = \mathbf{y}^{(i-1)} - \hat{g}_i\hat{\mathbf{T}}_i\mathbf{x}_p, \tag{33}$$

and it is used as the new observation for estimating parameters of the next path [17], [18], [19], [21]. As explained in [19] and [21], this procedure allows for IPI cancellation.

Algorithm 1 Proposed Correlation-Based Method for Channel Estimation

Input: $\mathbf{y},\ P,\ L_h,\ L_{\max},\ K_{\max}$

$\mathbf{y}^{(0)} = \mathbf{y}$

for $i = 1$ **to** P **do**

$\mathbf{Y}^{(i-1)} = \mathrm{vec}_{M,N}^{-1}\left(\mathbf{y}^{(i-1)}\right)$

$\hat{L}_i, \hat{K}_i = \arg\max_{(L,K)\in\mathcal{S}} \left|[\mathbf{Y}^{(i-1)}]_{m_p+L,\, n_p+K}\right|^2$

$\hat{\tilde{k}}_i^{(0)} = 0$

for $h = 1$ **to** L_h **do**

$\Delta k^{(h)} = 1/(2N_k)^h$

$\kappa^* = \arg\max_{\kappa} \left|\mathbf{x}_p^{\mathsf{H}} \mathbf{Q}^{\top}(\hat{L}_i)\mathbf{Q}^{\mathsf{H}}\left(\hat{K}_i + \kappa\Delta k^{(h)}\right)\mathbf{y}^{(i-1)}\right|$

$\hat{\tilde{k}}_i^{(h)} = \hat{\tilde{k}}_i^{(h-1)} + \Delta k^{(h)}\kappa^*$

$\hat{k}_i = \hat{K}_i + \hat{\tilde{k}}_i^{(L_h)}$

$\mathbf{y}_d^{(i-1)} = \mathbf{Q}^{\mathsf{H}}(\hat{k}_i)\,\mathbf{y}^{(i-1)}$

$\hat{\tilde{l}}_i^{(0)} = 0$

for $h = 1$ **to** L_h **do**

$\Delta l^{(h)} = 1/(2N_l)^h$

$\ell^* = \arg\max_{\ell} \left|\mathbf{x}_p^{\mathsf{H}} \mathbf{Q}^{\top}\left(\hat{L}_i + \ell\Delta l^{(h)}\right)\mathbf{y}_d^{(i-1)}\right|$

$\hat{\tilde{l}}_i^{(h)} = \hat{\tilde{l}}_i^{(h-1)} + \Delta l^{(h)}\ell^*$

$\hat{l}_i = \hat{L}_i + \hat{\tilde{l}}_i^{(L_h)}$

$\hat{\mathbf{T}}_i = \mathbf{Q}(\hat{k}_i)\,\mathbf{Q}^*(\hat{l}_i)$

$\hat{g}_i = \dfrac{\left(\hat{\mathbf{T}}_i\mathbf{x}_p\right)^{\mathsf{H}}\mathbf{y}^{(i-1)}}{E_p}$

$\mathbf{y}^{(i)} = \mathbf{y}^{(i-1)} - \hat{g}_i\,\hat{\mathbf{T}}_i\mathbf{x}_p$

Output: $\hat{\mathbf{H}}_{\mathrm{DD}} = \sum_{i=1}^{P} \hat{g}_i \hat{\mathbf{T}}_i$

The pseudocode of the proposed low-complexity disjoint DD correlation-based channel estimation method is provided in Algorithm 1.

Remark 3: The proposed channel parameter estimation algorithm leverages the sparsity of $\mathbf{Q}(a)$ to reduce computational complexity, as characterized in Proposition 1. This sparse structure arises when M is an integer multiple of N. Conversely, if this condition is not met, the $\mathbf{Q}(a)$ matrix becomes denser, and the sparsity property can no longer be exploited to reduce computational complexity. Nevertheless, since the unitary property of $\mathbf{Q}(a)$ remains intact, the proposed algorithm remains applicable, albeit at the cost of increased complexity.

C. ESTIMATION OF P: DL-AIDED MODEL ORDER SELECTION

In practical ISAC scenarios, the number of resolvable reflectors P is unknown. Iterative channel estimation algorithms often rely on a SC [17], [18], [19], [20], [21], [24] to estimate P and detect multiple paths. A conventional approach relies on defining a threshold based on the energy of the residual vector in (33). Specifically, when the energy of $\mathbf{y}^{(i)}$ falls below a designated tolerance value, the iterative process terminates, and the estimated number of propagation paths, $\hat{P}$, is determined by the total number of iterations performed. However, this approach raises the following concerns:

1) *Threshold-dependent accuracy*: The performance of an iterative channel estimation algorithm that uses a SC to estimate P heavily depends on the choice of the convergence tolerance parameter. To minimize estimation error, an exhaustive search for the optimal threshold is often necessary [17].
2) *IPI-induced estimation/detection trade-off*: When a SC-based approach is used, a lower threshold may reduce channel estimation error, but it can also lead to an overestimation of P. Conversely, a threshold optimized to correctly identify the number of paths may not be ideal for minimizing the overall estimation error. This discrepancy arises because IPI limits the accuracy of the estimated paths. In more detail, IPI leads to residual pilot peaks that may be interpreted as small amplitude paths, leading to an overestimation of P if the threshold is not properly set. Therefore, a refinement procedure should be carried out to discard false alarms [21], increasing complexity.
3) *Poor detection capabilities at low SNR*: At low signal-to-noise ratios, small-amplitude paths may be missed if their amplitudes become comparable to the noise level. This occurs because a few high-amplitude paths may be sufficient to meet the stopping criterion, thereby masking the presence of weaker paths.

To this end, the following DL-aided scheme is proposed to estimate P. The estimation of P is formulated as a single-label multi-class classification problem: a multipath channel belongs to the class $c \in \mathcal{C}$ if it is characterized by $P^{(c)}$ propagation paths, where $\mathcal{C}$ denotes the set of considered model orders. A FNN is trained to solve this classification task. Specifically, the element-wise magnitude of the received pilot vector, denoted as $|\mathbf{y}| = \mathbf{y} \odot \mathbf{y}^* \in \mathbb{R}^{MN\times 1}$, is provided as input to the network.[3] This choice is physically motivated by the fact that the key information regarding the number of propagation paths is inherently embedded in the power profile of the received pilot signal, where distinct multipath components manifest as energy peaks in the delay-Doppler domain, whereas the phase information is highly volatile and less indicative of the model order.

To formalize the processing pipeline of the FNN, let L denote the total number of layers. The real-valued feature vector $|\mathbf{y}|$ is fed into the first hidden layer, yielding the activation vector $\mathbf{a}^{(1)} \in \mathbb{R}^{N_1\times 1}$

$$\mathbf{a}^{(1)} = \sigma_{\mathrm{ReLU}}\left(\mathbf{W}^{(1)}|\mathbf{y}| + \mathbf{b}^{(1)}\right), \tag{34}$$

[3]Since the input layer dimension of the FNN is fixed to MN, changing the OTFS frame size requires modifying the input layer and retraining the network. This represents a known architectural constraint when applying standard deep neural networks (DNNs) to multi-carrier systems [24], [27], [31].

where $\mathbf{W}^{(1)} \in \mathbb{R}^{N_1 \times MN}$ and $\mathbf{b}^{(1)} \in \mathbb{R}^{N_1 \times 1}$ represent the weight matrix and the bias vector of the first layer, respectively, while $\sigma_{\text{ReLU}}(\cdot) = \max(0, \cdot)$ denotes the element-wise rectified linear unit (ReLU) activation function. For any subsequent hidden layer $l \in \{2, \ldots, L-1\}$, the operational model transitions recursively as

$$\mathbf{a}^{(l)} = \sigma_{\text{ReLU}}\left(\mathbf{W}^{(l)}\mathbf{a}^{(l-1)} + \mathbf{b}^{(l)}\right), \tag{35}$$

where $\mathbf{W}^{(l)} \in \mathbb{R}^{N_l \times N_{l-1}}$ and $\mathbf{b}^{(l)} \in \mathbb{R}^{N_l \times 1}$ are the weights and biases corresponding to the l-th layer.

To map the output of the final hidden layer into a mathematically sound posterior probability distribution over the $C = |\mathcal{C}|$ classes, the output layer utilizes the Softmax activation function. The resulting network output vector $\mathbf{p} \in \mathbb{R}^C$ is mathematically defined as

$$\mathbf{p} = \sigma_{\text{soft}}\left(\mathbf{W}^{(L)}\mathbf{a}^{(L-1)} + \mathbf{b}^{(L)}\right), \tag{36}$$

where $\mathbf{W}^{(L)} \in \mathbb{R}^{C \times N_{L-1}}$ and $\mathbf{b}^{(L)} \in \mathbb{R}^{C \times 1}$ denote the parameters of the final layer, and the c-th element of $\mathbf{p}$ is computed via the Softmax operator $\sigma_{\text{soft}}(\cdot)$ as follows

$$[\mathbf{p}]_c = \frac{e^{[\mathbf{W}^{(L)}\mathbf{a}^{(L-1)} + \mathbf{b}^{(L)}]_c}}{\sum_{k=1}^{C} e^{[\mathbf{W}^{(L)}\mathbf{a}^{(L-1)} + \mathbf{b}^{(L)}]_k}}. \tag{37}$$

The term $[\mathbf{p}]_c$ represents the estimated probability that the channel contains a number of paths corresponding to the c-th class. After training, the final estimate of P is obtained during inference via the following selection rule

$$\hat{P} = \arg\max_{c \in \mathcal{C}} [\mathbf{p}]_c. \tag{38}$$

Remark 4: It is worth noting that if the actual number of propagation paths in the channel exceeds the maximum cardinality predefined during the design phase, the proposed FNN will inevitably saturate, leading to a degradation in estimation accuracy. However, this behavior does not represent a specific drawback of the DL-based approach; rather, it constitutes an intrinsic limitation of parametric channel estimation frameworks in general. Even in conventional SC-based methods, a maximum allowable number of paths must be strictly enforced [17], [18], [19], [20], [21], [24]. This hard limit is practically necessary not only to bound computational complexity but also to prevent algorithmic divergence, such as infinite iterative loops triggered by noise-induced residual peaks. Consequently, the saturation under an unmodeled number of paths is a structural constraint shared by both the SC-based baselines and the proposed scheme, reflecting the fundamental trade-offs inherent to parametric channel modeling.

D. MULTI-TARGET PARAMETER ESTIMATION AT SENSING RECEIVER

In the considered ISAC scenario, the transmitted signal is backscattered by a given number of sensing targets in the environment. The radar parameters (range and velocity) of the sensing targets can be estimated at the sensing receiver by processing the received signal in (22) using the correlation method. The target range and velocity can be obtained by estimating the RTD and Doppler frequency associated with the target. In particular, since the co-located sensing receiver has access to all transmit data symbols in (22), the integer DDs can be estimated as

$$\hat{L}_i, \hat{K}_i = \arg\max_{(L,K)\in\mathcal{S}} \left|\mathbf{x}^{\mathsf{H}}\mathbf{Q}^{\top}(L)\mathbf{Q}^{\mathsf{H}}(K)\mathbf{y}^{(i-1)}\right|, \tag{39}$$

by maximizing the magnitude of the correlation between the transmitted data frame $\mathbf{x}$ and the estimated data frame $\mathbf{Q}^{\top}(L)\mathbf{Q}^{\mathsf{H}}(K)\mathbf{y}^{(i-1)}$ obtained as output of a MF. Afterwards, the fractional delay and Doppler of the target are estimated and refined separately using the disjoint hierarchical approach in (28) and (31). Multi-target detection is achieved by using (38) and iterating this procedure as described in Section IV-B. Finally, ranges and velocities of the targets can be obtained using

$$\hat{d}_i = \frac{\hat{l}_i \Delta\tau}{2} c, \;\; \hat{v}_i = \frac{\hat{k}_i \Delta\nu}{2 f_c} c. \tag{40}$$

E. COMPLEXITY

Table 1 presents a complexity comparison between the proposed channel estimation method, referred to as FNN-based correlation method (CM-FNN), the high-IPI-resilient PIPIC approach proposed in [21], and the two step estimator (TSE) algorithm proposed in [17] and [18]. The complexity of the proposed method is primarily driven by the hierarchical refinement of channel parameters. Specifically, the complexity of the proposed method increases with the sum of N_k and N_l due to the separate DD estimation, similarly to the TSE method [17], [18]. On the other hand, the complexity of channel estimation algorithms that perform joint DD estimation (e.g., PIPIC) [17], [20], [21], [24] grows with the product of the number of delay and Doppler grid points, as they rely on a 2D search. Moreover, regarding model order selection, the proposed FNN-based approach requires higher complexity than conventional SC-based approaches in order to provide a substantial performance gain at low SNR.

F. CRAMÉR-RAO LOWER BOUND FOR RADAR SENSING

To evaluate the fundamental limits of the monostatic radar parameter estimation under arbitrary data transmission, the expected Cramér-Rao lower bound (CRLB) is derived. Without loss of generality, a single-target scenario is considered. The vector of radar kinematic parameters is defined by $\boldsymbol{\theta} = [\tau, \nu]^T$. Following the normalization assumptions maintained throughout the paper, the complex path gain is normalized to unity ($g = 1$), removing it from the active parameter search space.

The discrete DD input-output relationship for the target echo in (22) is expressed as

$$\mathbf{y} = \boldsymbol{\mu}(l, k) + \mathbf{w}, \tag{41}$$

where $\boldsymbol{\mu}(l, k) = \mathbf{T}\mathbf{x} = \mathbf{Q}(k)\mathbf{Q}^{*}(l)\mathbf{x}$ is the noiseless received signal vector.

Since the communication data vector $\mathbf{x}$ is random and varies across frames, the Fisher information matrix (FIM)

TABLE 1. Complexity comparison for channel estimation.

	Proposed CM-FNN	TSE [17], [18]	PIPIC [21]
Estimation of P	FNN-based $\mathcal{O}((MN)^2)$	SC-based $\mathcal{O}(MN)$	SC-based $\mathcal{O}(MN)$
Estimation of L_i, K_i	joint $\mathcal{O}((L_{\max}+1)(2K_{\max}+1))$	joint $\mathcal{O}((L_{\max}+1)(2K_{\max}+1))$	joint $\mathcal{O}((L_{\max}+1)(2K_{\max}+1))$
Estimation of $\tilde{l}_i, \tilde{k}_i$	disjoint $\mathcal{O}(L_h N_k) + \mathcal{O}(L_h N_l)$	disjoint $\mathcal{O}(N_k) + \mathcal{O}(N_l)$	joint $\mathcal{O}(L_h N_l N_k)$
Estimation of g_i	$\mathcal{O}(MN)$	$\mathcal{O}(MN)$	$\mathcal{O}(PMN) + \mathcal{O}(P^3)$
Global refinement	no	no	yes

$\mathbf{J} \in \mathbb{R}^{2\times 2}$ is formalized by taking the expectation with respect to the signaling statistics of $\mathbf{x}$

$$[\mathbf{J}]_{p,q} = \frac{2}{\sigma^2}\mathbb{E}_{\mathbf{x}}\left[\Re\left\{\left(\frac{\partial \boldsymbol{\mu}(l,k)}{\partial \theta_p}\right)^H \frac{\partial \boldsymbol{\mu}(l,k)}{\partial \theta_q}\right\}\right]. \tag{42}$$

Under the assumption of independent identically distributed (iid) information symbols, the data covariance matrix evaluates to $\mathbf{C}_{\mathrm{x}} = \mathbb{E}\left[\mathbf{x}\mathbf{x}^{\mathsf{H}}\right] = E_s\mathbf{I}_{MN}$, where E_s is the average energy per symbol. Utilizing the linear expectation property $\mathbb{E}[\mathbf{x}^H\mathbf{A}\mathbf{x}] = \mathrm{tr}(\mathbf{A}\mathbb{E}[\mathbf{x}\mathbf{x}^H])$, the elements of the average 2×2 kinematic FIM can be analytically rewritten as

$$[\mathbf{J}]_{p,q} = \frac{2E_s}{\sigma^2}\Re\left\{\mathrm{tr}\left(\left(\frac{\partial \mathbf{T}}{\partial \theta_p}\right)^H \frac{\partial \mathbf{T}}{\partial \theta_q}\right)\right\}. \tag{43}$$

The analytical dependency on the continuous delay and Doppler metrics is embedded within the core diagonal matrix $\mathbf{D}$, as shown by (20). Let $\tilde{\mathbf{F}} = \mathbf{F}_N \otimes \mathbf{I}_M$ and define the phase derivative operator as $\mathbf{D}' = \mathrm{diag}\left(\left[j\frac{2\pi q}{MN}z^q\right]_{q=0}^{MN-1}\right)$. The partial derivatives of the structural sparse parameter matrices $\mathbf{Q}(k)$ and $\mathbf{Q}^*(l)$ with respect to their normalized arguments are explicitly given by

$$\frac{\partial \mathbf{Q}(k)}{\partial k} = \tilde{\mathbf{F}}\mathbf{D}'\mathbf{D}^{k-1}\mathbf{F}_{MN}^H\tilde{\mathbf{F}}, \tag{44}$$

$$\frac{\partial \mathbf{Q}^*(l)}{\partial l} = \tilde{\mathbf{F}}(\mathbf{D}')^*(\mathbf{D}^*)^{l-1}\mathbf{F}_{MN}^H\tilde{\mathbf{F}}. \tag{45}$$

Applying the chain rule with respect to the continuous physical parameters τ and ν, the exact algebraic partial derivatives for the channel transfer matrix $\mathbf{T}$ are obtained

$$\frac{\partial \mathbf{T}}{\partial \tau} = \frac{1}{\Delta\tau}\mathbf{Q}(k)\left(\frac{\partial \mathbf{Q}^*(l)}{\partial l}\right), \tag{46}$$

$$\frac{\partial \mathbf{T}}{\partial \nu} = \frac{1}{\Delta\nu}\left(\frac{\partial \mathbf{Q}(k)}{\partial k}\right)\mathbf{Q}^*(l). \tag{47}$$

Upon constructing the 2×2 kinematic FIM, the fundamental lower bounds for the target range $\hat{d}$ and radial velocity $\hat{v}$ are directly extracted from the diagonal elements of the inverted matrix $\mathbf{J}^{-1}$ via the physical mapping relations

$$\mathrm{CRLB}(d) = \frac{c^2}{4}[\mathbf{J}^{-1}]_{1,1}, \tag{48}$$

$$\mathrm{CRLB}(v) = \frac{c^2}{4f_c^2}[\mathbf{J}^{-1}]_{2,2}. \tag{49}$$

V. DATA DETECTION AT COMMUNICATION RECEIVER

In the ISAC scenario under consideration, the single-antenna communication receiver processes the pilot frame to obtain the estimate $\hat{\mathbf{H}}_{\mathrm{DD}}$. It then uses this estimate to equalize incoming data frames within the channel coherence time. The transmitter is assumed to send iid information symbols. Therefore, $\mathbf{C}_{\mathrm{x}} = \mathbb{E}\left[\mathbf{x}\mathbf{x}^{\mathsf{H}}\right] = E_s\mathbf{I}_{MN}$, where E_s is the average energy per symbol. Since each symbol encodes $\log_2(Q)$ bits, the average energy per bit is given by $E_b = E_s/\log_2(Q)$. The data signal-to-noise ratio is defined as the ratio between the average signal power and the average noise power

$$\mathrm{SNR}_d = \frac{E_s/NT}{M\Delta f N_0} = \frac{E_s}{N_0}. \tag{50}$$

Equivalently, $\mathrm{SNR}_d = \mathrm{tr}(\mathbf{C}_{\mathrm{x}})/\mathrm{tr}(\mathbf{C}_{\mathrm{w}}) = E_s/\sigma^2$, leading to a noise variance of $\sigma^2 = N_0$.

In this section, a low-complexity version of the Landweber method [45], [46] that exploits the sparsity of $\mathbf{Q}(a)$ is presented for OTFS detection. In particular, a path-wise version of the Landweber method, named IMFC, is developed to reduce complexity. The proposed data detector is directly connected to the channel estimation framework developed in the Sections III and IV. In fact, the estimated path parameters $\{\hat{g}_i, \hat{k}_i, \hat{l}_i\}_{i=1}^{\hat{P}}$ provide a path-wise representation of the estimated DD channel through the same structurally sparse matrices $\mathbf{Q}(\hat{k}_i)\mathbf{Q}^*(\hat{l}_i)$ introduced in Section III. Rather than reconstructing and processing the full DD channel matrix, the proposed detector directly exploits this parametric representation, the structural sparsity and the DD decomposition to enable low-complexity data detection, leading to the path-wise IMFC formulation developed below. Channel estimation and data detection are therefore regarded as two consecutive stages of the same structure-exploiting receiver architecture. The section is structured as follows: first, the LMMSE equalization method is reviewed and considered as the benchmark; then, Landweber method is presented and the proposed IMFC algorithm is introduced and analyzed.

A. LMMSE DETECTOR

The LMMSE equalizer has been extensively investigated [39], [40], [42], with various low-complexity variants proposed to achieve satisfactory detection performance. Although alternative OTFS detection schemes, such as MP, offer low complexity under ideal integer conditions, they

become practically infeasible in real-world scenarios with fractional delay and Doppler shifts due to severe energy leakage and dense factor graph connectivity. Consequently, the LMMSE detector serves as the most appropriate and reliable benchmark for evaluating receiver performance in realistic fractional-DD environments. The traditional LMMSE equalizer for (14) is given by [11], [47]

$$\hat{\mathbf{x}} = \mathbf{C}_{\mathrm{x}}\mathbf{H}_{\mathrm{DD}}^{\mathsf{H}}\left(\mathbf{H}_{\mathrm{DD}}\mathbf{C}_{\mathrm{x}}\mathbf{H}_{\mathrm{DD}}^{\mathsf{H}} + \mathbf{C}_{\mathrm{w}}\right)^{-1}\mathbf{y}, \tag{51}$$

where $\hat{\mathbf{x}}$ denotes the estimated information symbols vector and the DD channel matrix is given as (19). Using (16), (50) and the symbol's independence assumption, the LMMSE estimate reduces to

$$\hat{\mathbf{x}} = \mathbf{H}_{\mathrm{DD}}^{\mathsf{H}}\left(\mathbf{H}_{\mathrm{DD}}\mathbf{H}_{\mathrm{DD}}^{\mathsf{H}} + \mathrm{SNR}_d^{-1}\mathbf{I}_{MN}\right)^{-1}\mathbf{y}. \tag{52}$$

B. PROPOSED IMFC DETECTOR BASED ON LANDWEBER METHOD

The Landweber method is a well-known iterative method for solving ill-posed linear systems of equations [45], [46]. In particular, given the noisy system in (14) and considering that $\mathbf{H}_{\mathrm{DD}}$ is typically not invertible, an estimate of $\mathbf{x}$ can be iteratively refined using the following Landweber update equations

$$\hat{\mathbf{x}}^{(n)} = \hat{\mathbf{x}}^{(n-1)} + \alpha\mathbf{H}_{\mathrm{DD}}^{\mathsf{H}}\boldsymbol{\mathcal{E}}^{(n-1)}, \tag{53}$$

$$\boldsymbol{\mathcal{E}}^{(n)} = \mathbf{y} - \mathbf{H}_{\mathrm{DD}}\hat{\mathbf{x}}^{(n)}, \tag{54}$$

where α is the step size and $\boldsymbol{\mathcal{E}}^{(n)}$ is the residue vector. The estimation error at time n is given as

$$\mathbf{e}^{(n)} = \hat{\mathbf{x}}^{(n)} - \mathbf{x}. \tag{55}$$

By replacing (54) in (53), the estimate at the n-th iteration becomes

$$\hat{\mathbf{x}}^{(n)} = \alpha\mathbf{H}_{\mathrm{DD}}^{\mathsf{H}}\mathbf{y} + \left(\mathbf{I}_{MN} - \alpha\mathbf{H}_{\mathrm{DD}}^{\mathsf{H}}\mathbf{H}_{\mathrm{DD}}\right)\hat{\mathbf{x}}^{(n-1)}. \tag{56}$$

By applying (56) recursively and assuming that $\hat{\mathbf{x}}^{(n)} = \mathbf{0}$, the estimate can be written as

$$\hat{\mathbf{x}}^{(n)} = \sum_{i=0}^{n-1}\left(\mathbf{I}_{MN} - \alpha\mathbf{H}_{\mathrm{DD}}^{\mathsf{H}}\mathbf{H}_{\mathrm{DD}}\right)^{i}\alpha\mathbf{H}_{\mathrm{DD}}^{\mathsf{H}}\mathbf{y}. \tag{57}$$

Thus, it can be noted that, if, as $n \to \infty$

$$\rho\left(\mathbf{I}_{MN} - \alpha\mathbf{H}_{\mathrm{DD}}^{\mathsf{H}}\mathbf{H}_{\mathrm{DD}}\right) < 1, \tag{58}$$

where it is reminded that $\rho\left(\mathbf{I}_{MN} - \alpha\mathbf{H}_{\mathrm{DD}}^{\mathsf{H}}\mathbf{H}_{\mathrm{DD}}\right)$ denotes the spectral radius of $\mathbf{I}_{MN} - \alpha\mathbf{H}_{\mathrm{DD}}^{\mathsf{H}}\mathbf{H}_{\mathrm{DD}}$, the algorithm converges [46]. Equivalently, from (58), it can be noted that the learning rate parameter (α) should satisfy

$$\alpha < \frac{2}{\rho(\mathbf{H}_{\mathrm{DD}}^{\mathsf{H}}\mathbf{H}_{\mathrm{DD}})}, \tag{59}$$

to guarantee algorithmic convergence. Moreover, the geometric series in (57) converges to

$$\sum_{i=0}^{+\infty}\left(\mathbf{I}_{MN} - \alpha\mathbf{H}_{\mathrm{DD}}^{\mathsf{H}}\mathbf{H}_{\mathrm{DD}}\right)^{i}$$

$$= \left(\mathbf{I}_{MN} - \left(\mathbf{I}_{MN} - \alpha\mathbf{H}_{\mathrm{DD}}^{\mathsf{H}}\mathbf{H}_{\mathrm{DD}}\right)\right)^{-1}$$

$$= \left(\alpha\mathbf{H}_{\mathrm{DD}}^{\mathsf{H}}\mathbf{H}_{\mathrm{DD}}\right)^{-1} = \frac{\left(\mathbf{H}_{\mathrm{DD}}^{\mathsf{H}}\mathbf{H}_{\mathrm{DD}}\right)^{-1}}{\alpha}. \tag{60}$$

Thus,

$$\hat{\mathbf{x}}^{(\infty)} = \lim_{n\to\infty}\hat{\mathbf{x}}^{(n)} = \left(\mathbf{H}_{\mathrm{DD}}^{\mathsf{H}}\mathbf{H}_{\mathrm{DD}}\right)^{-1}\mathbf{H}_{\mathrm{DD}}^{\mathsf{H}}\mathbf{y} \tag{61}$$

Therefore, the iterative Landweber method converges to the least squares (LS) solution [45]. Moreover, replacing (55) in (61), the output error becomes

$$\mathbf{e}^{(\infty)} = \lim_{n\to\infty}\mathbf{e}^{(n)} = \left(\mathbf{H}_{\mathrm{DD}}^{\mathsf{H}}\mathbf{H}_{\mathrm{DD}}\right)^{-1}\mathbf{H}_{\mathrm{DD}}^{\mathsf{H}}\mathbf{w}. \tag{62}$$

Hence, denoting $\mathbf{H}_{\mathrm{DD}}^{\dagger} = \left(\mathbf{H}_{\mathrm{DD}}^{\mathsf{H}}\mathbf{H}_{\mathrm{DD}}\right)^{-1}\mathbf{H}_{\mathrm{DD}}^{\mathsf{H}}$ the Moore-Penrose pseudoinverse of the channel matrix $\mathbf{H}_{\mathrm{DD}}$, the mean squared error (MSE) after convergence is

$$\begin{aligned}\mathbb{E}\left[\|\mathbf{e}^{(\infty)}\|^2\right] &= \mathbb{E}\left[\|\mathbf{H}_{\mathrm{DD}}^{\dagger}\mathbf{w}\|^2\right] = \mathbb{E}\left[\mathrm{tr}\left(\mathbf{H}_{\mathrm{DD}}^{\dagger}\mathbf{w}\mathbf{w}^{\mathsf{H}}(\mathbf{H}_{\mathrm{DD}}^{\dagger})^{\mathsf{H}}\right)\right]\\ &= \mathrm{tr}\left(\mathbf{H}_{\mathrm{DD}}^{\dagger}\mathbb{E}\left[\mathbf{w}\mathbf{w}^{\mathsf{H}}\right](\mathbf{H}_{\mathrm{DD}}^{\dagger})^{\mathsf{H}}\right)\\ &= \sigma^2\mathrm{tr}\left(\mathbf{H}_{\mathrm{DD}}^{\dagger}(\mathbf{H}_{\mathrm{DD}}^{\dagger})^{\mathsf{H}}\right)\\ &= \sigma^2\mathrm{tr}\left((\mathbf{H}_{\mathrm{DD}}^{\mathsf{H}}\mathbf{H}_{\mathrm{DD}})^{-1}\right).\end{aligned} \tag{63}$$

From (22), it is possible to decompose the Landweber iterative update equations path-wise as follows

$$\hat{\mathbf{x}}^{(n)} = \hat{\mathbf{x}}^{(n-1)} + \alpha\sum_{i=1}^{P} g_i^{*}\mathbf{Q}^{\top}(l_i)\mathbf{Q}^{\mathsf{H}}(k_i)\boldsymbol{\mathcal{E}}^{(n-1)}, \tag{64}$$

$$\boldsymbol{\mathcal{E}}^{(n)} = \mathbf{y} - \sum_{i=1}^{P} g_i\mathbf{Q}(k_i)\mathbf{Q}^{*}(l_i)\hat{\mathbf{x}}^{(n)}. \tag{65}$$

Therefore, the Landweber method can be decomposed in P separate branches in which the residue vector passes through a MF $\mathbf{Q}^{\mathsf{H}}(k_i)$ tuned at the Doppler affecting the i-th path and then it passes through a MF $\mathbf{Q}^{\top}(l_i)$ tuned at the delay affecting the i-th path. In this way, P incremental updates are obtained and combined using maximal ratio combining (MRC) to maximize the SNR. This path-wise interpretation of the Landweber method is called IMFC. The advantage of this approach is that, from Proposition 1, each row of $\mathbf{Q}(a)$ contains only M nonzero elements. Therefore, the complexity of the matrix by vector multiplication requires a complexity of $\mathcal{O}(M^2N)$ rather than $\mathcal{O}\left((MN)^2\right)$ as in the Landweber method.

The proposed IMFC equalizer is summarized in Algorithm 2. Theoretically, strictly satisfying the convergence condition in (59) requires calculating the exact spectral radius of $\mathbf{H}_{\mathrm{DD}}^{H}\mathbf{H}_{\mathrm{DD}}$ for each received frame. However, computing this maximum eigenvalue entails a non-negligible computational cost. Therefore, for practicality, the step size α is instead obtained using a time-decaying model as $\alpha^{(n)} = \frac{\alpha_0}{1+\beta n}$, where α_0 is the initial step size and β is the decay factor. While a fixed empirical α_0 might momentarily violate the theoretical bound for specific severe channel realizations, a properly tuned β forces the step size to rapidly decrease. This mechanism acts as a safety net: even if an initial

TABLE 2. Complexity comparison for data detection under different parameter regimes.

	Grid Condition	Channel Profile	Per-iteration Complexity	Overall Complexity	Advantage vs LMMSE	Advantage vs Landweber
LMMSE	Any	Any	N/A	$\mathcal{O}\big((MN)^3\big)$	–	–
Landweber	Any	Any	$\mathcal{O}\big((MN)^2\big)$	$\mathcal{O}\big(n(MN)^2\big)$	Yes (if $n \ll MN$)	–
Proposed IMFC (Sparse regime)	$M = qN$ $(q \in \mathbb{N})$	Sparse $(P < N)$	$\mathcal{O}(PM^2N)$	$\mathcal{O}(nPM^2N)$	Yes	Yes
Proposed IMFC (Dense regime)	$M \neq qN$	Rich scattering $(P \gg N)$	$\mathcal{O}\big(P(MN)^2\big)$	$\mathcal{O}\big(nP(MN)^2\big)$	Yes (if $n \ll \frac{MN}{P}$)	No

Algorithm 2 Proposed IMFC Detector

Input: $\mathbf{y},\ \epsilon,\ n_{\max},\ \alpha_0,\ \beta$
$\hat{\mathbf{x}}^{(0)} = \mathbf{0},\ \boldsymbol{\mathcal{E}}^{(0)} = \mathbf{y},\ \alpha = \alpha_0,\ n = 0$
while $n \leq n_{\max}$ *AND* $\|\boldsymbol{\mathcal{E}}^{(n)}\| \geq \epsilon$ **do**
  $n = n + 1$
  for $i = 1$ **to** P **do**
    $\boldsymbol{\mathcal{E}}_{D,i}^{(n-1)} = \mathbf{Q}^{\mathsf{H}}(k_i)\boldsymbol{\mathcal{E}}^{(n-1)}$
    $\boldsymbol{\mathcal{E}}_{d,i}^{(n-1)} = \mathbf{Q}^{\top}(l_i)\boldsymbol{\mathcal{E}}_{D,i}^{(n-1)}$
  $\hat{\mathbf{x}}^{(n)} = \hat{\mathbf{x}}^{(n-1)} + \alpha \sum_{i=1}^{P} g_i^* \boldsymbol{\mathcal{E}}_{d,i}^{(n-1)}$
  for $i = 1$ **to** P **do**
    $\hat{\mathbf{x}}_{d,i}^{(n)} = \mathbf{Q}^*(l_i)\hat{\mathbf{x}}^{(n)}$
    $\hat{\mathbf{x}}_{D,i}^{(n)} = \mathbf{Q}(k_i)\hat{\mathbf{x}}_{d,i}^{(n)}$
  $\boldsymbol{\mathcal{E}}^{(n)} = \mathbf{y} - \sum_{i=1}^{P} g_i \hat{\mathbf{x}}_{D,i}^{(n)}$
  $\alpha = \frac{\alpha_0}{1+\beta n}$
Output: $\hat{\mathbf{x}}$

transient divergence occurs, the algorithm swiftly enters the theoretical convergence region, ensuring convergence without the need for expensive spectral radius evaluations. Moreover, the procedure is iterated for a finite number of steps until $\|\boldsymbol{\mathcal{E}}^{(n)}\| < \epsilon$ or $n = n_{\max}$.

C. COMPLEXITY: LMMSE VS IMFC

The complexity of the traditional LMMSE equalizer is in the order of $\mathcal{O}\big((MN)^3\big)$ due to matrix inversion. On the other hand, the complexity of the standard Landweber method is $\mathcal{O}\big(n(MN)^2\big)$, increasing linearly with the number of iterations. Instead, the path-wise IMFC equalizer directly exploits the structural sparsity of $\mathbf{Q}(a)$ as established in Proposition 1 and Remark 3. Specifically, when M is an integer multiple of N ($M = qN$ with $q \in \mathbb{N}$), each row of $\mathbf{Q}(a)$ contains strictly M non-zero elements, enabling highly efficient sparse matrix-vector multiplications.

Under this structured parameter regime and assuming a sparse multipath profile ($P < N$), the overall computational complexity of the proposed IMFC reduces to $\mathcal{O}(nPM^2N)$ (or $\mathcal{O}(PM^2N)$ per iteration). It can be concluded that, provided $n \ll MN^2/P$, the proposed IMFC achieves a drastically lower computational load than the traditional LMMSE equalizer and standard iterative solvers (which generally incur at least $\mathcal{O}\big((MN)^2\big)$ per iteration [48]).

However, in unconstrained parameter regimes where M is not an integer multiple of N, the matrix $\mathbf{Q}(a)$ transitions into a denser configuration, causing the per-iteration complexity of IMFC to scale back toward the standard non-sparse solver complexity of $\mathcal{O}\big((MN)^2\big)$ per iteration. This behavior stems from the fact that IMFC relies on path-wise operations exploiting the structural sparsity of $\mathbf{Q}(a)$, whereas general iterative solvers depend on the entire channel matrix $\mathbf{H}_{\text{DD}}$, which is typically non-sparse for fractional channel parameters. A comparative overview of the computational complexity under different operational conditions is summarized in Table 2.

VI. SIMULATION RESULTS

In this section, numerical results are reported to validate the proposed estimation/detection methodologies. The transmitter works at carrier frequency $f_c = 5$ GHz. The subcarrier spacing is $\Delta f = 15$ kHz, hence the time slot duration is $T = 66.67\ \mu$s.

A. SIMULATION SCENARIO

A channel with $P = 4$ Rayleigh faded paths is considered. The power delay profile (PDP) is $[0, 2.4, 5, 7]\,\mu$s with relative powers $[0, -1, -5, -7]$ dB. The Doppler shifts of all paths are generated assuming Jakes' Doppler power spectrum (DPS) using $\nu_i = \nu_{\max}\cos(\theta_i)$, where $\theta_i \sim \mathcal{U}[0, 2\pi]$. The maximum user equipment (UE) speed is $v_{\max} = 500$ km/h, leading to a maximum Doppler spread of $\nu_{\max} = \frac{v_{\max}}{c} f_c = 2.3164$ kHz. Unless otherwise stated, the OTFS frame is characterized by $M = 64$ subcarriers and $N = 16$ time slots. Crucially, this setup represents a genuinely fractional DD channel scenario. Considering the grid resolutions $\Delta\tau \approx 1.0417\,\mu$s and $\Delta\nu \approx 937.5$ Hz, the corresponding normalized path delays are $l_i = [0, 2.304, 4.800, 6.720]$, clearly exhibiting non-zero off-grid components. Likewise, the normalized Doppler shifts $k_i = \nu_i/\Delta\nu$ vary continuously within the non-integer range $[-2.47, 2.47]$, ensuring that both delay and Doppler shifts feature fractional components. Grid parameters for estimation in Algorithm 1 are set to $N_l, N_k = 7$.[4] Finally, the convergence

[4]The parameters N_k, N_l, and L_h are interconnected: a smaller grid requires more hierarchical levels to reach the same resolution, while a larger L_h increases the recursive overhead. The minimum density of the initial grid is constrained by the Hessian of the cost function, as it must be sufficient to capture the main lobe of the objective function to ensure convergence of subsequent refinement steps. Here, N_k, N_l are chosen according to this reasoning and to optimize estimation accuracy while lowering complexity.

parameters of Algorithm 2 are set to $\alpha_0 = 1$ and $\beta = 0.05$. These values are selected empirically to strike a balance between fast initial convergence (promoted by a relatively large α_0) and algorithmic stability (ensured by the decay factor β). It is worth noting that in a practical real-time system, if packet decoding errors occur due to a step-size mismatch with the instantaneous channel conditions, these parameters can be easily adjusted and lowered on-the-fly. A detailed mechanism for the dynamic optimization of the learning rate is out of the scope of this paper.

Within this simulation scenario, the system operates as described in Section II.[5]

B. NETWORK ARCHITECTURE AND TRAINING

This section details the training process for the proposed FNN model order selection scheme. The training dataset $\mathcal{D}$ is a collection of S independent samples. Each sample consists of a pair containing the received pilot observation vector and its corresponding ground-truth label, represented as a one-hot vector

$$\mathcal{D} = \left\{(|\mathbf{y}^{(s)}|, \mathbf{p}^{(s)})\right\}_{s=1}^{S}, \tag{66}$$

where $|\mathbf{y}^{(s)}| \in \mathbb{R}^{MN\times 1}$ is the s-th received pilot frame and $\mathbf{p}^{(s)} \in \{0,1\}^C$ is the label vector such that $[\mathbf{p}^{(s)}]_c = 1$ if the s-th channel realization contains $P^{(c)}$ paths. The FNN parameters are optimized by minimizing the categorical cross-entropy loss function over the training set

$$\mathcal{L}(\boldsymbol{\theta}) = -\frac{1}{S}\sum_{s=1}^{S}\sum_{c=1}^{C}[\mathbf{p}^{(s)}]_c \ln([\hat{\mathbf{p}}^{(s)}]_c), \tag{67}$$

where $\boldsymbol{\theta}$ denotes the set of network weights and biases, and $\hat{\mathbf{p}}^{(s)} = f_{\text{FNN}}(|\mathbf{y}^{(s)}|;\boldsymbol{\theta})$ is the probability vector predicted by the output layer.

The DL network for model order selection is assumed to have two hidden layers. The input dimension is MN, as $|\mathbf{y}|$ is provided as input, while the output dimension is C, as the vector $\mathbf{p}$ is provided as output. The number of neurons per hidden layer is $\{\frac{MN}{4}, \frac{MN}{8}\}$, and each hidden layer employs a ReLU activation function. The output layer utilizes a softmax activation function to compute probabilities, following the classification problem formulation. For the simulations, the proposed DL architecture is trained on a dataset comprising 3×6000 samples, collected from three distinct datasets (each containing 6000 samples) generated at discrete SNR_p levels (5 dB, 10 dB, and 15 dB, respectively). Each training sample is created assuming channels with $P \sim \mathcal{U}[2,5]$ paths, a uniform PDP, and continuous uniform random path delays. Crucially, while training is restricted to these three discrete SNR values, a uniform PDP, and random delays, the network is evaluated over a continuous SNR range under a non-uniform PDP with specific off-grid fractional delays, as detailed in Section VI-A, thereby evaluating its generalization capability against mismatched power profiles and operating conditions. The training process runs for 2000 epochs with a mini-batch size of 1000. The learning rate is initially set to 0.001 and is reduced by a factor of 0.9 every 50 epochs. This simple architecture for the proposed DL-aided scheme is chosen to prioritize low computational latency during inference, ensuring that the model order selection remains efficient for real-time ISAC applications. Moreover, FNNs have been shown to be suitable for simple classification tasks [50], which aligns with the objective of the proposed DL-based approach.

[5]In our simulations, the frame duration is set to $NT \approx 1$ ms. Given that the geometric coherence time of the channel parameters (i.e., path gains, delays, and Doppler shifts) is typically on the order of tens of milliseconds [11], [49], these parameters remain effectively stationary across multiple consecutive frames. This physical property justifies the adopted transmission strategy where a single pilot frame is followed by multiple data frames.

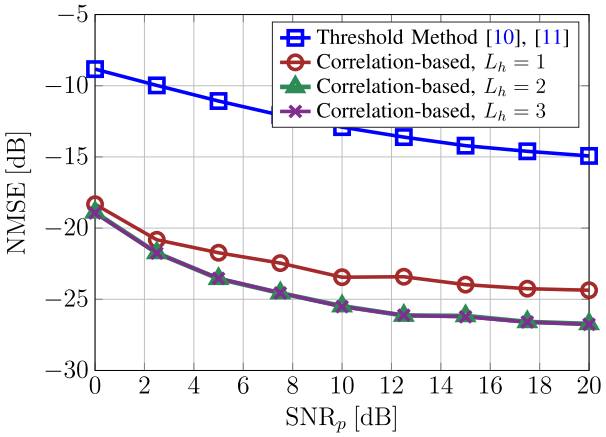


FIGURE 3. Comparison of the threshold method [10], [11] and the proposed correlation-based method in Algorithm 1 with prior knowledge of P. The normalized MSE vs pilot SNR is shown for different values of L_h.

C. CHANNEL ESTIMATION PERFORMANCE AT COMMUNICATION RECEIVER

In the considered scenario, different performance metrics are evaluated to measure channel estimation performance and are listed as follows.

1) NMSE VS PILOT SNR

The accuracy of channel estimation algorithms is evaluated using the normalized mean squared error (NMSE), computed as

$$\text{NMSE} = \mathbb{E}\left[\frac{\|\mathbf{H}_{\text{DD}} - \hat{\mathbf{H}}_{\text{DD}}\|_F^2}{\|\mathbf{H}_{\text{DD}}\|_F^2}\right]. \tag{68}$$

Fig. 3 illustrates the normalized mean squared error (NMSE) as a function of pilot SNR for the proposed method in Algorithm 1, considering different numbers of hierarchical levels ($L_h = 1, 2, 3$) with prior knowledge of P. As a baseline, the conventional threshold method [10], [11] is also reported. As expected, the performance of the baseline method is limited by IPI, achieving a minimum NMSE of -15 dB at $\text{SNR}_p = 20$ dB. Conversely, the proposed correlation-based method attains a lower NMSE. Specifically, when $L_h = 1$, the proposed method provides a performance gain of nearly 10 dB over the entire SNR_p range compared to the baseline method. Increasing the number of hierarchical

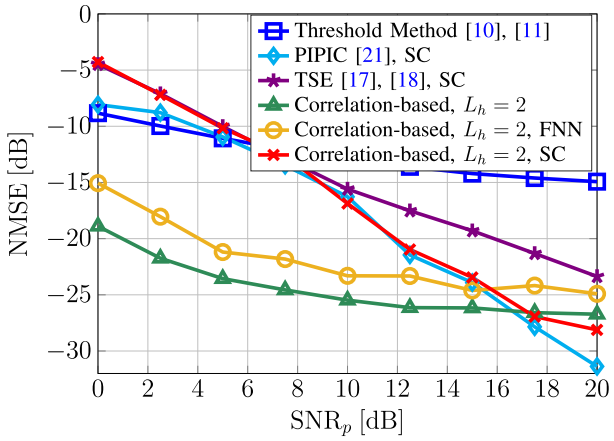


FIGURE 4. Comparison of the proposed FNN-based estimation of P against the conventional SC-based approach. The normalized MSE vs pilot SNR is shown for the optimum number of hierarchical levels $L_h = 2$.

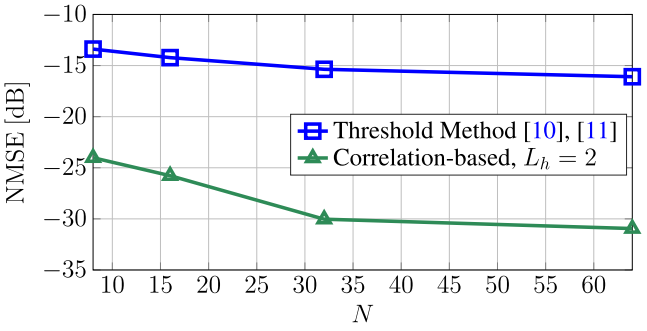


FIGURE 5. Channel estimation accuracy measured through the NMSE is shown as a function of the number of Doppler bins. Both the baseline threshold method and the proposed correlation-based method with $L_h = 2$ are shown.

levels to $L_h = 2$ yields an additional gain of approximately 2 dB at sufficiently high SNR$_p$. However, using $L_h = 3$ does not result in further performance improvements beyond those obtained with $L_h = 2$, making $L_h = 2$ the optimal choice. Instead, selecting $L_h = 3$ increases computational complexity without enhancing estimation accuracy.

Fig. 4 shows the NMSE as a function of pilot SNR when estimating P. The proposed FNN-based approach in (38) is compared with the SC-based approach (specifically, the TSE method proposed in [17] and [18] performing disjoint DD estimation and the PIPIC proposed in [21] that performs joint DD estimation). Additionally, the performance of the proposed approach with SC-based estimation of P is reported. The threshold method and the proposed correlation-based method with prior knowledge of P are included as upper and lower benchmarks for comparison. As expected, due to the generalization capabilities of the neural network, the proposed FNN-based approach significantly outperforms the SC-based approach at low SNR$_p$, providing more stable estimation accuracy across different SNR$_p$ values and exhibiting a performance loss of only 2-3 dB compared to the ideal case where P is known. Furthermore, for SNR$_p$ in the range $[0, 6]$ dB, the SC-based approach underperforms the threshold method. This is because, at very low SNR$_p$, the SC-based approach fails to detect lower-amplitude paths that are masked by the SC, allowing the simpler threshold method to achieve a lower estimation error. On the other hand, at high SNR$_p$, SC-based approaches achieve better performance at the cost of overestimating P. Additionally, in mid-range SNR$_p$ conditions, the performance of PIPIC is nearly identical to that of the proposed approach with SC-based estimation of P. Thus, in the proposed approach, disjoint estimation reduces complexity without sacrificing performance. On the other hand, performance of the TSE, which also performs disjoint DD estimation, is lower than that of the PIPIC and the proposed correlation method. Specifically, at high SNR the performance gain of the proposed correlation based method against the TSE is about 4-5 dB of NMSE. This performance gain arises because the disjoint DD estimation in the TSE algorithm relies on an approximate ML formulation that is valid only for large OTFS frames [17], [18]. In contrast, our proposed method leverages an exact algebraic separability that remains robust even in scenarios with significant IPI.

2) NMSE VS OTFS FRAME SIZE

The estimation accuracy varies as the number of delay-Doppler bins changes. Given that a low value of N is used in the considered scenario, it is particularly relevant to evaluate estimation accuracy as a function of the number of time slots N.

Fig. 5 presents the NMSE as a function of the number of Doppler bins for both the threshold method [10], [11] and the proposed correlation-based method. Simulations are conducted with a fixed $M = 64$ and at SNR$_p = 15$ dB. It can be observed that, since the threshold method is primarily limited by IPI, increasing N from 8 to 64 provides a maximum performance gain of 3 dB. Conversely, the proposed correlation-based method accounts for IPI, resulting in a performance gain of 6 dB when increasing N. Furthermore, the proposed correlation-based method achieves an improvement of nearly 15 dB compared to the baseline method when $M = N = 64$.

3) MODEL ORDER SELECTION

As the proposed approach uses the FNN for model order selection, a comparison of the average number of detected paths for both the baseline SC-based approach and the proposed FNN-based approach is illustrated in Fig. 6. Specifically, the figure shows the average number of detected paths as a function of SNR$_p$. As expected, the neural network is able to accurately estimate the correct number of paths on average. In contrast, the SC-based approach significantly underestimates P at low SNR$_p$. Therefore, the proposed FNN-based approach effectively improves estimation performance in low SNR$_p$ conditions.

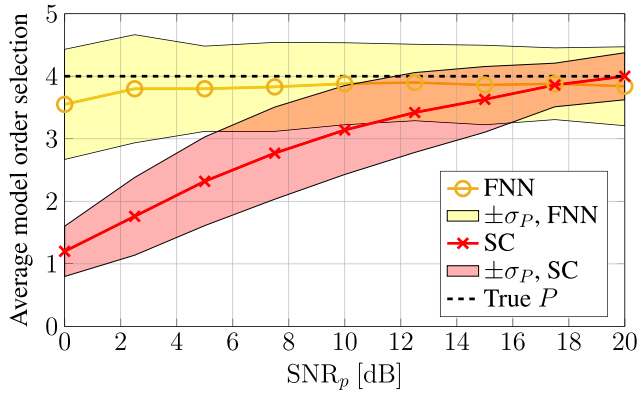


FIGURE 6. Model order selection comparison between the conventional SC-based approach against the proposed FNN-based approach. The true value of P is also shown for the comparison.

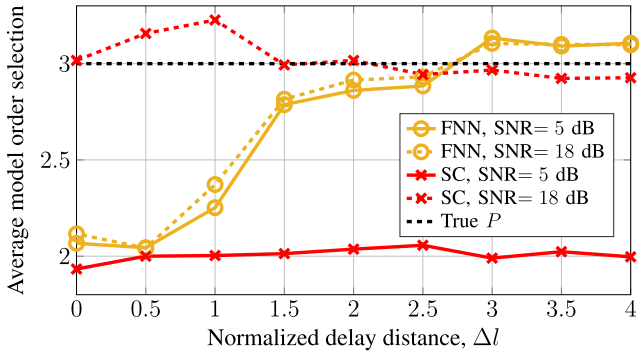


FIGURE 7. Average number of detected paths versus delay distance for the SC-based approach and the proposed FNN-based method at different SNR levels (SNR$_p$ = 5 dB and SNR$_p$ = 18 dB). The dashed line represents the true value of P.

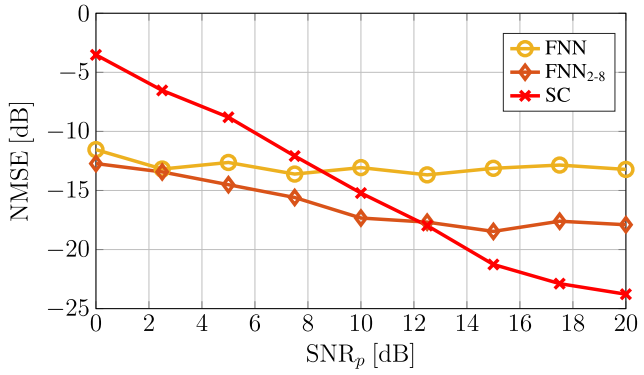


FIGURE 8. Comparison of the proposed FNN-based model order selection scheme against the SC-based approach. The NMSE performance is shown against pilot SNR using the proposed correlation-based channel estimation algorithm with $L_h = 2$. Finally, FNN denotes the DL scheme, trained as discussed in Section VI-B; while FNN$_{2\text{-}8}$ denotes the same FNN trained with a dataset including channels with $P \in [2, 8]$.

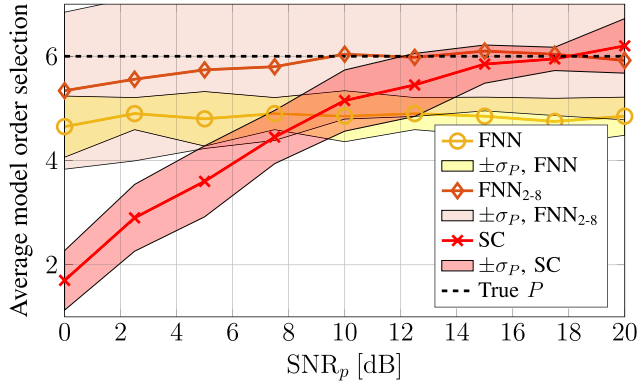


FIGURE 9. Model order selection comparison between the conventional SC-based approach against the proposed FNN-based approach in a channel with $P = 6$ paths. Here, FNN$_{2\text{-}8}$ denotes the same FNN trained with a dataset including channels with $P \in [2, 8]$.

4) FNN RESOLUTION ANALYSIS

In this section, the resolution capabilities of the proposed FNN-based model order selection are investigated. Fig. 7 illustrates the average number of detected paths as a function of the delay distance between paths for both the SC-based approach and the proposed FNN architecture. The scenario includes $P = 3$ paths, where the first path delay is kept fixed ($l_1 = 0$), while the second and third paths are positioned to test the resolution limits of the estimator. Specifically, the second path delay is set to $l_2 = \tau_2/\Delta\tau$ (with $\tau_2 = 2.4\mu$s), and the third path is placed at $l_3 = l_2 + \Delta l$, where Δl is a normalized delay distance. The PDP is defined as $[0, -1, -5]$ dB, resulting in a 4 dB dynamic range between the third and second paths. As observed in the simulation results, the SC-based approach suffers from significant path underestimation at low SNR (SNR$_p$ = 5 dB), regardless of the delay distance, as the weaker path is often masked by noise and IPI. Conversely, at high SNR (SNR$_p$ = 18 dB), the SC-based method tends to overestimate the number of paths when the delay distance is small due to the IPI that creates residual peaks in the DD domain. In contrast, the FNN-based approach demonstrates superior robustness. Even at low SNR, the neural network accurately identifies the correct number of paths as the delay distance increases beyond a certain threshold. The generalization capabilities of the FNN allow it to effectively distinguish between closely spaced paths and noise-induced artifacts, providing a more stable model order selection under varying SNR conditions. These results further highlight that the proposed DL-aided architecture enhances path detection performance in challenging high-IPI and low-SNR scenarios.

5) FNN PERFORMANCE UNDER INCREASED MODEL ORDER

Since, as described in Section VI-B, the FNN scheme has been trained on a limited dataset, in Fig. 8 and 9 channel estimation and model order selection performance is investigated in a channel with $P = 6$ paths to analyze the impact of FNN behavior when faced with an unseen class. Since the model is constrained by its final layer to a fixed set of outcomes, the estimated number of paths is expected to saturate at the maximum trained cardinality (i.e., $\hat{P} = 5$), as the network cannot infer a new output class beyond its predefined architectural limits. This behavior is highlighted

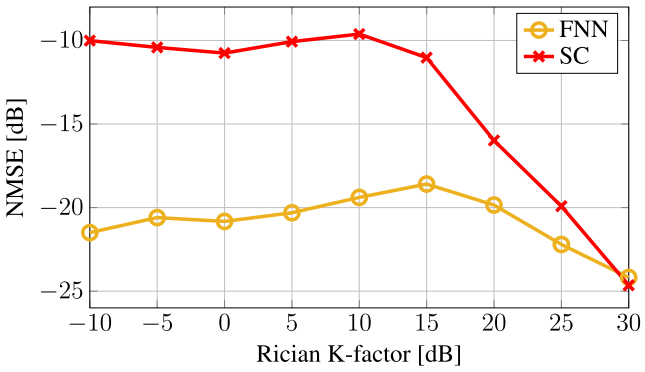


FIGURE 10. Comparison of the proposed FNN-based model order selection scheme against the SC-based approach under Rician fading. The NMSE performance is shown against Rician K factor using the proposed correlation-based channel estimation algorithm with $L_h = 2$.

in Fig. 9, where it can be noted that the average number of paths detected by the FNN is around 5, regardless of the SNR. On the other hand, the SC-based approach exhibits SNR-dependent model order selection capabilities, underestimating the number of paths at low SNR. Fig. 9 shows also the average number of paths detected by the same FNN described in Section VI-B and trained with a dataset with the same size (18000 samples) but with a larger number of classes, specifically $P \sim \mathcal{U}[2, 8]$. It can be observed that the model order selection capabilities are increased as the FNN is actually capable of detecting the correct number of paths on average. On the other hand, it can be noted that the variance of the estimate is increased since the same dataset size has been used for a larger number of classes. These model order selection capabilities affect the channel estimation error, as depicted in Fig. 8, where it can be noted that at low SNR the FNN-based approach allows achieving lower NMSE. Moreover, the use of the same FNN, trained with a large number of classes leads to a NMSE gain of almost 5 dB at high SNR.

6) NMSE VS RICIAN K-FACTOR

The robustness of the proposed FNN-based channel estimation method against varying propagation conditions is investigated by considering a Rician fading channel. While the Rayleigh model remains the reference high-mobility scenario in this work, this Rician experiment is introduced specifically as a generalization test for the neural network. Since the FNN is trained exclusively under Rayleigh fading statistics, evaluating it in the presence of a line-of-sight (LoS) component allows us to assess its robustness against a controlled statistical mismatch in the fading distribution. Specifically, the impact of a predominant LoS component on the NMSE is evaluated by varying the Rician K-factor. For this analysis, the SNR is fixed at $\text{SNR}_p = 5$ dB to consider a low-SNR regime, while the Rician K-factor is varied from -10 dB to 30 dB. The channel model consists of $P = 4$ propagation paths, where the delay and Doppler shifts are generated according to the methodology described in Section VI-A. The channel coefficients are modeled such that the first path ($i = 1$) contains the LoS component. Specifically, the i-th coefficient is expressed as

$$g_i = \begin{cases} \sqrt{\dfrac{K}{K+1}} e^{j\theta} + w_i, & i = 1 \\ w_i, & i > 1 \end{cases}, \tag{69}$$

where $w_i \sim \mathcal{CN}\left(0, \frac{1}{K+1}\right)$ represents the diffuse scattering component and $\theta \sim \mathcal{U}[0, 2\pi]$ is the LoS phase. Finally, channel gains are normalized according to Section IV-A. Fig. 10 shows the NMSE against the Rician K factor for the proposed correlation based channel estimation algorithm. It can be noted that, the SC-based scheme achieves low NMSE when the LoS component is dominant, as the LoS is correctly identified and the diffuse scattering component are typically missed, since they fall below the noise level. On the other hand, when the channel starts becoming Rayleigh faded (as K decreases), performance of the SC-based algorithm drops and the NMSE increases to -10 dB. Conversely, the FNN-based scheme achieves much lower and stable NMSE across the entire range of K, with a performance gain of about 10 dB for lower values of K.

D. SENSING PERFORMANCE AT THE ISAC TRANSCEIVER

To evaluate sensing performance, a scenario with a target at a range of $d = 300$ m and a velocity of $v = 70$ km/h is considered. The OTFS frame parameters are set to $M = N = 32$, and the transmitter employs quadrature amplitude modulation (QAM) signaling with $Q = 4$.

1) SINGLE-TARGET RANGE/VELOCITY RMSE VS RADAR SNR

The radar parameter estimation performance of the proposed ISAC sensing algorithm is assessed using the root mean squared error (RMSE) of the target's range and velocity.

Fig. 11 presents the range and velocity RMSEs for different values of radar SNR. The radar SNR is defined as $\text{SNR}_{\text{rad}} = \frac{|g_i|^2}{N_0}$, where $|g_i|^2$ represents the target power. Performance is evaluated for different values of $L_h = 1, 2, 3$ and compared against the CRLB and the PIPIC method [21], which performs joint DD estimation, in order to investigate whether there is any performance loss when shifting from a joint 2D parameter search to the proposed low-complexity dis- joint DD estimation. It can be observed that increasing L_h allows the proposed approach to achieve performance close to the CRLB. Specifically, sub-meter localization accuracy is attainable at SNR_{rad} values above 10 dB when $L_h \geq 2$. Moreover, the proposed method achieves the exact same performance as the joint DD estimation performed by PIPIC. Thus, the proposed disjoint DD estimation framework guarantees no performance loss while drastically lowering the computational complexity from a 2D grid search to two independent 1D line searches.

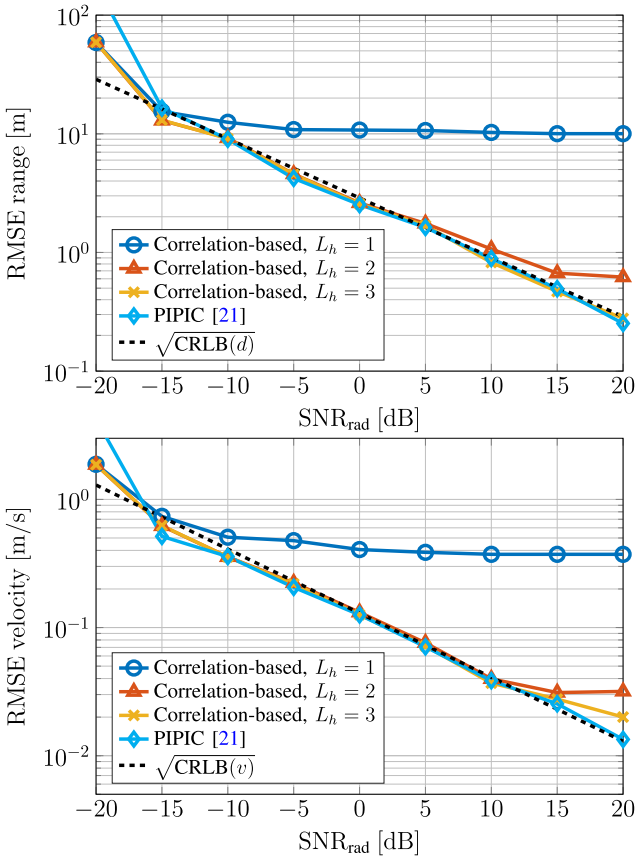


FIGURE 11. The range/velocity RMSE against radar SNR are shown for different values of L_h. The CRLB is reported as a lower bound to radar parameter estimation.

2) TARGET DISCRIMINATION IN MULTI-TARGET SCENARIOS

As described in Section IV-D, the proposed FNN architecture is also applicable to multi-target detection. In this context, Fig. 7 provides insights into DL-based multi-target detection performance. Specifically, it can be observed that the proposed FNN exhibits consistent detection capabilities regardless of the SNR. Conversely, the performance of the SC-based approach relies heavily on SNR conditions. The proposed FNN is capable of resolving targets that are at least one resolution cell apart across all SNR levels. In contrast, the SC fails to distinguish adjacent targets, incorrectly identifying them as a single entity in low SNR scenarios even with larger delay separations.

E. COMMUNICATION PERFORMANCE

The receiver is assumed to execute a channel estimation algorithm to obtain a channel estimate, followed by an equalization method to compensate for the channel. Subsequently, a symbol-by-symbol ML detector is employed to make hard decisions.

1) BER VS E_B/N_0

Communication performance is evaluated in terms of the BER as a function of the signal-to-noise ratio per bit

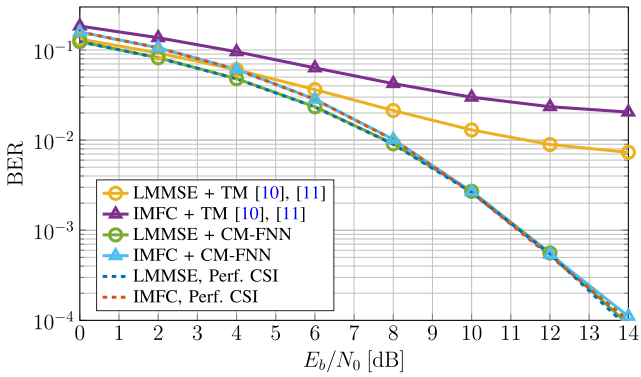


FIGURE 12. The bit error rate as a function of the signal-to-noise ratio per bit is shown for both the LMMSE and proposed IMFC equalizers in the following cases: perfect CSI at the receiver, imperfect CSI estimated through the baseline threshold method and through the proposed FNN-aided correlation-based method. The imperfect CSI curves serve as a sensitivity analysis to channel estimation errors.

(E_b/N_0). Fig. 12 illustrates the BER as a function of E_b/N_0 for both the LMMSE and the proposed IMFC equalizers. In the simulations, the transmitter is assumed to use a 4-QAM constellation, while the IMFC equalizer operates with $\epsilon = \frac{\sqrt{MN\sigma^2}}{2}$ and $n_{\max} = 50$. The performance under perfect channel state information (CSI) knowledge at the receiver is provided as a lower bound on the probability of error, serving as a reference for comparing the two equalization techniques. It can be observed that, at sufficiently high SNR, the proposed IMFC equalizer achieves a BER comparable to that of the conventional LMMSE equalizer. In order to investigate the sensitivity of the proposed IMFC equalizer to channel estimation errors, Fig. 12 also compares BER performance under imperfect CSI, where channel estimates are obtained from different estimation algorithms. Specifically, the BER performance using LMMSE and the proposed IMFC equalizers is shown for channel estimates obtained via the conventional threshold method (TM) [10], [11] and the proposed CM-FNN, assuming SNR$_p$ = 18 dB. It can be noted that the proposed channel estimation method in Algorithm 1 achieves performance nearly equivalent to the ideal case of perfect CSI for both the LMMSE and IMFC equalizers. In contrast, the conventional TM method is constrained by IPI and, therefore, fails to compensate for channel impairments when IPI is significant. Consequently, the proposed CM-FNN channel estimation algorithm achieves a substantial performance gain over the conventional TM approach.

2) AVERAGE NUMBER OF ITERATIONS FOR THE IMFC EQUALIZER

To assess the complexity of the proposed equalization scheme compared to the LMMSE, the average number of iterations is analyzed as a function of E_b/N_0. Fig. 13 presents the average number of iterations required by the proposed IMFC equalizer under three conditions: perfect CSI at the receiver, and imperfect CSI estimated using the conventional TM and the proposed CM-FNN. It can be observed that the complexity of the IMFC equalizer remains unaffected by

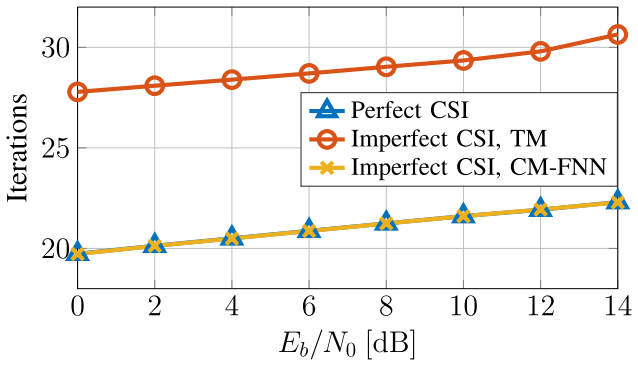


FIGURE 13. The average number of iterations for the proposed IMFC equalizer as a function of the signal-to-noise ratio per bit. Both perfect CSI and imperfect CSI cases are considered using the baseline threshold method and the proposed FNN-aided correlation method.

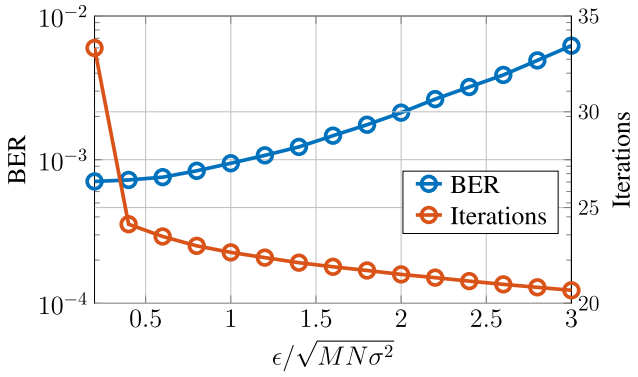


FIGURE 14. The influence of the threshold ϵ on the average number of iterations and BER for the proposed IMFC equalizer.

imperfect CSI when using the proposed channel estimation algorithm. Conversely, complexity increases when CSI is estimated using the conventional TM method. However, it is worth noting that the average number of iterations required by the IMFC equalizer remains significantly lower than MN^2/P. Therefore, as discussed in Section V-C, the proposed IMFC equalizer offers substantially lower complexity than the conventional LMMSE while achieving nearly the same BER performance.

3) INFLUENCE OF THE THRESHOLD

The choice of the threshold ϵ for the stopping criterion of the IMFC equalizer plays a crucial role in balancing the performance/complexity trade-off. Specifically, a higher threshold is expected to reduce complexity at the cost of degraded BER performance, whereas a lower threshold may enhance BER performance but at the expense of increased complexity. Fig. 14 illustrates the average number of iterations and BER performance of the proposed IMFC equalizer for different values of the threshold ϵ. Simulations are conducted at $E_b/N_0 = 12$ dB. It can be observed that BER decreases as ϵ is reduced. However, the improvement stabilizes around $\epsilon/\sqrt{MN\sigma^2} = 0.5$. Conversely, complexity starts to increase significantly when the threshold is further reduced. Therefore, the optimal threshold choice is $\epsilon = 0.5\sqrt{MN\sigma^2}$. This analysis justifies the selected threshold value used for evaluating BER performance.

VII. CONCLUSION

In this work, the DD input-output relationship for OTFS-ISAC with RCP is formulated by establishing an exact, non-asymptotic algebraic decoupling of the fractional channel parameters. By directly exploiting the inherent cyclic matrix structure induced by the RCP architecture, the channel matrix factorization holds as a strict mathematical identity rather than an asymptotic approximation (e.g., relying on large frame dimensions $N, M \to \infty$). Consequently, this structural separation enables a low-complexity disjoint DD estimation framework that operates completely independent of the transmitted DD symbol sequence, thereby eliminating the need for restrictive pilot-pattern constraints or dedicated guard zones typical of conventional schemes. The DD channel effects are represented through a unitary sparse matrix, enabling simple correlation-based channel estimation using matched filtering. To further enhance performance, a FNN-based architecture is introduced to estimate the number of propagation paths, overcoming the limitations of conventional stopping criteria and enhancing performance under low SNR conditions. Simulation results demonstrate that the proposed FNN-aided correlation-based approach achieves accurate channel estimation and BER performance comparable to the ideal case with perfect CSI knowledge. Sensing performance is evaluated by computing the RMSE, and the results show that increasing the number of hierarchical levels allows performance close to the CRLB to be achieved. Therefore, disjoint estimation allows reducing complexity without degrading performance, compared to joint estimation algorithms. Furthermore, by exploiting the sparsity of the DD parameter matrix, a reduced-complexity equalizer based on Landweber method, called IMFC algorithm, is proposed for channel equalization. This approach achieves BER performance comparable to that of the conventional LMMSE equalizer but with significantly lower complexity.

Future works will consider disjoint fractional DD estimation in multi-antenna OTFS receivers using superimposed pilot schemes for PAPR reduction and increased spectral efficiency compared to exclusive pilot schemes. Furthermore, future research will investigate frame-size-independent model order selection architectures to overcome the input-dimension constraints of the proposed FNN scheme. Additionally, exploring iterative receiver architectures that perform joint channel estimation and data detection represents a promising direction to further enhance OTFS system performance.

APPENDIX A
PROOF OF THEOREM 1

The cyclic shift property in (9) inherited by the RCP allows a frequency-domain representation of the transmitted signal [34], [37], thus $s([t-\tau_i]_{NT}) = \mathcal{F}^{-1}\{S(f)e^{-j2\pi f\tau_i}\}$. Sampling (9) at T/M and discretizing frequency (with spacing $\Delta f/N$),

the following samples are obtained

$$\mathbf{r} = \sum_{i=1}^{P} g_i[\mathbf{F}_{MN}^{\mathsf{H}}(\mathbf{F}_{MN}\mathbf{s} \odot \mathbf{b}(\tau_i))] \odot \mathbf{c}(\nu_i) + \mathbf{n}, \tag{70}$$

where $\mathbf{b}(\tau_i) = \left[e^{-j2\pi q \frac{\Delta f}{N}\tau_i}\right]_{q=0}^{MN-1}$ and $\mathbf{c}(\nu_i) = \left[e^{j2\pi q \frac{T}{M}\nu_i}\right]_{q=0}^{MN-1}$ are the frequency-domain and temporal steering vectors, respectively. By normalizing channel parameters as $l_i = \frac{\tau_i}{\Delta\tau} = L_i + \tilde{l}_i$, $k_i = \frac{\nu_i}{\Delta\nu} = K_i + \tilde{k}_i$, the expression for the elements of $\mathbf{d}(\tau_i)$ and $\mathbf{c}(\nu_i)$, it is possible to notice that

$$e^{-j2\pi q \frac{\Delta f}{N}\tau_i} = e^{-j2\pi q \frac{\Delta f}{N}(L_i+\tilde{l}_i)\Delta\tau} = \left(e^{-j\frac{2\pi}{MN}q}\right)^{L_i+\tilde{l}_i}, \tag{71}$$

$$e^{j2\pi q \frac{T}{M}\nu_i} = e^{j2\pi q \frac{T}{M}(K_i+\tilde{k}_i)\Delta\nu} = \left(e^{j\frac{2\pi}{MN}q}\right)^{K_i+\tilde{k}_i}. \tag{72}$$

Therefore, the two Hadamard products in (70) can be expressed as a matrix by vector product by defining the diagonal matrix $\mathbf{D} = \text{diag}\left\{\left[e^{j\frac{2\pi}{MN}q}\right]_{q=0}^{MN-1}\right\}$ as

$$\mathbf{r} = \sum_{i=1}^{P} g_i \mathbf{D}^{K_i}\mathbf{D}^{\tilde{k}_i}\mathbf{F}_{MN}^{\mathsf{H}}(\mathbf{D}^*)^{L_i}(\mathbf{D}^*)^{\tilde{l}_i}\mathbf{F}_{MN}\mathbf{s} + \mathbf{n}. \tag{73}$$

Finally, (11) is obtained from (10) and (73).

APPENDIX B
PROOF OF COROLLARY 1

If delays and Dopplers are multiple of delay and Doppler resolutions, it can be noticed that $\mathbf{D}^{\tilde{k}_i} = \mathbf{I}_{MN}$ and $(\mathbf{D}^*)^{\tilde{l}_i} = \mathbf{I}_{MN}$. Hence, (11) reduces to

$$\mathbf{H} = \sum_{i=1}^{P} g_i \mathbf{D}^{K_i}\mathbf{F}_{MN}^{\mathsf{H}}(\mathbf{D}^*)^{L_i}\mathbf{F}_{MN}. \tag{74}$$

Moreover, it can be noted that $\mathbf{F}_{MN}^{\mathsf{H}}(\mathbf{D}^*)^{L_i}\mathbf{F}_{MN}$ is the eigenvalue decomposition of the circulant matrix $\mathbf{\Pi}^{L_i}$. In fact, $\mathbf{\Pi}^{L_i} = \mathbf{F}_{MN}^{\mathsf{H}}\mathbf{\Lambda}\mathbf{F}_{MN}$ where the diagonal matrix $\mathbf{\Lambda}$ is given as

$$\begin{aligned}\mathbf{\Lambda} &= \text{diag}\left(\sqrt{MN}\mathbf{F}_{MN}\mathbf{e}_{[L_i+1]_{MN}}\right) \\ &= \text{diag}\left(\left[z^{-qL_i}\right]_{q=0}^{MN-1}\right) = (\mathbf{D}^*)^{L_i}.\end{aligned} \tag{75}$$

APPENDIX C
PROOF OF PROPOSITION 1

The generic element of $\mathbf{Q}(a)$ is obtained by

$$[\mathbf{Q}(a)]_{p,q} = \sum_{s=0}^{MN-1}[\tilde{\mathbf{F}}]_{p,s}\sum_{t=0}^{MN-1}[\tilde{\mathbf{D}}(a)]_{s,t}[\tilde{\mathbf{F}}]_{t,q}, \tag{76}$$

where $\tilde{\mathbf{F}} = \mathbf{F}_N \otimes \mathbf{I}_M$, $\tilde{\mathbf{D}}(a) = \mathbf{D}^a\mathbf{F}_{MN}^{\mathsf{H}}$ and

$$\begin{aligned}[\tilde{\mathbf{F}}]_{t,q} &= [\mathbf{F}_N]_{\lfloor t/M\rfloor,\lfloor q/M\rfloor}[\mathbf{I}_M]_{\text{mod}(t,M),\text{mod}(q,M)} \\ &= [\mathbf{F}_N]_{\lfloor t/M\rfloor,\lfloor q/M\rfloor}\delta_{\text{mod}(t,M),\text{mod}(q,M)},\end{aligned} \tag{77}$$

$$[\tilde{\mathbf{D}}(a)]_{s,t} = \sum_{r=0}^{MN-1}[\mathbf{D}^a]_{s,r}[\mathbf{F}_{MN}^{\mathsf{H}}]_{r,t} = [\mathbf{D}^a]_{s,s}[\mathbf{F}_{MN}^{\mathsf{H}}]_{s,t} = \frac{e^{j\frac{2\pi s(a+t)}{MN}}}{\sqrt{MN}}. \tag{78}$$

Plugging (78) and (77) back in (76)

$$\begin{aligned}[\mathbf{Q}(a)]_{p,q} = &\frac{1}{N\sqrt{MN}}\sum_{s=0}^{MN-1}[\mathbf{F}_N]_{\lfloor p/M\rfloor,\lfloor s/M\rfloor}\delta_{\text{mod}(p,M),\text{mod}(s,M)} \\ &\sum_{t=0}^{MN-1}e^{j\frac{2\pi s(a+t)}{MN}}[\mathbf{F}_N]_{\lfloor t/M\rfloor,\lfloor q/M\rfloor}\delta_{\text{mod}(t,M),\text{mod}(q,M)}.\end{aligned} \tag{79}$$

By introducing new indices k_1 and k_2 ranging from 0 to $N-1$ and substituting s and t as $s = k_1M + \text{mod}(p,M)$ and $t = k_2M + \text{mod}(q,M)$ in (79), the final form presented in (23) in Proposition 1 is obtained. Moreover, (23) can be rewritten as

$$\begin{aligned}\left[\mathbf{Q}(a)\right]_{p,q} = &\frac{1}{N\sqrt{MN}} \\ &\sum_{k_1=0}^{N-1}e^{-j\frac{2\pi\lfloor p/M\rfloor k_1}{N}}e^{j\frac{2\pi}{MN}\left(k_1M+\text{mod}(p,M)\right)\left(a+\text{mod}(q,M)\right)} \\ &\sum_{k_2=0}^{N-1}e^{j\frac{2\pi k_2}{N}\left(k_1M+\text{mod}(p,M)-\lfloor q/M\rfloor\right)}.\end{aligned} \tag{80}$$

Finally, using the fact that $\sum_{k'=0}^{N-1}e^{j\frac{2\pi k' u}{N}} = N$ if u is an integer multiple of N and zero otherwise, it can be shown that, if M is an integer multiple of N, the element $\left[\mathbf{Q}(a)\right]_{p,q}$ is non-zero, for a fixed row p, for M consecutive values of q.

REFERENCES

[1] M. Giordani, M. Polese, M. Mezzavilla, S. Rangan, and M. Zorzi, "Toward 6G networks: Use cases and technologies," *IEEE Commun. Mag.*, vol. 58, no. 3, pp. 55–61, Mar. 2020.

[2] Z. Zhang et al., "6G wireless networks: Vision, requirements, architecture, and key technologies," *IEEE Veh. Technol. Mag.*, vol. 14, no. 3, pp. 28–41, Sep. 2019.

[3] R. Hadani et al., "Orthogonal time frequency space modulation," in *Proc. IEEE Wireless Commun. Netw. Conf. (WCNC)*, Mar. 2017, pp. 1–6.

[4] T. Wang, J. G. Proakis, E. Masry, and J. R. Zeidler, "Performance degradation of OFDM systems due to Doppler spreading," *IEEE Trans. Wireless Commun.*, vol. 5, no. 6, pp. 1422–1432, Jun. 2006.

[5] R. Hadani and A. Monk, "OTFS: A new generation of modulation addressing the challenges of 5G," 2018, *arXiv:1802.02623*.

[6] S. K. Mohammed, R. Hadani, A. Chockalingam, and R. Calderbank, "OTFS—A mathematical foundation for communication and radar sensing in the delay-Doppler domain," *IEEE BITS Inf. Theory Mag.*, vol. 2, no. 2, pp. 36–55, Nov. 2022.

[7] L. Gaudio, M. Kobayashi, G. Caire, and G. Colavolpe, "On the effectiveness of OTFS for joint radar parameter estimation and communication," *IEEE Trans. Wireless Commun.*, vol. 19, no. 9, pp. 5951–5965, Sep. 2020.

[8] P. Wei, Y. Xiao, W. Feng, N. Ge, and M. Xiao, "Characterizing the peak-to-average power ratio of OTFS signals: A large system analysis," *IEEE Trans. Wireless Commun.*, vol. 21, no. 6, pp. 3705–3720, Jun. 2022.

[9] A. Correas-Serrano, N. Petrov, M. Gonzalez-Huici, and A. Yarovoy, "Emerging trends in radar: OTFS-based radar for integrated sensing and communications systems," *IEEE Aerosp. Electron. Syst. Mag.*, vol. 40, no. 6, pp. 102–107, Jun. 2025.

[10] P. Raviteja, K. T. Phan, and Y. Hong, "Embedded pilot-aided channel estimation for OTFS in delay–Doppler channels," *IEEE Trans. Veh. Technol.*, vol. 68, no. 5, pp. 4906–4917, May 2019.

[11] Y. Hong, T. Thaj, and E. Viterbo, *Delay-Doppler Communications: Principles and Applications*. Amsterdam, The Netherlands: Elsevier, 2022.

[12] O. K. Rasheed, G. D. Surabhi, and A. Chockalingam, "Sparse delay-Doppler channel estimation in rapidly time-varying channels for multiuser OTFS on the uplink," in *Proc. IEEE 91st Veh. Technol. Conf. (VTC-Spring)*, May 2020, pp. 1–5.

[13] L. Zhao, W.-J. Gao, and W. Guo, "Sparse Bayesian learning of delay-Doppler channel for OTFS system," *IEEE Commun. Lett.*, vol. 24, no. 12, pp. 2766–2769, Dec. 2020.

[14] Z. Wei, W. Yuan, S. Li, J. Yuan, and D. W. K. Ng, "Off-grid channel estimation with sparse Bayesian learning for OTFS systems," *IEEE Trans. Wireless Commun.*, vol. 21, no. 9, pp. 7407–7426, Sep. 2022.

[15] Y. Zhang, Q. Zhang, C. He, L. Jing, T. Zheng, and C. Yuen, "Sparse Bayesian learning approach for OTFS channel estimation with fractional Doppler," *IEEE Trans. Veh. Technol.*, vol. 73, no. 11, pp. 16846–16860, Nov. 2024.

[16] X. Li, Y. Liang, Z. Zhou, and P. Fan, "Fractional delay-Doppler channel estimation for OTFS systems based on segmentation technique and sparse Bayesian learning," *IEEE Commun. Lett.*, vol. 29, no. 5, pp. 1067–1071, May 2025.

[17] I. A. Khan and S. K. Mohammed, "Low complexity channel estimation for OTFS modulation with fractional delay and Doppler," 2021, *arXiv:2111.06009*.

[18] I. A. Khan and S. K. Mohammed, "A low-complexity OTFS channel estimation method for fractional delay-Doppler scenarios," *IEEE Wireless Commun. Lett.*, vol. 12, no. 9, pp. 1484–1488, Sep. 2023.

[19] V. Yogesh, S. R. Mattu, and A. Chockalingam, "Low-complexity delay-Doppler channel estimation in discrete Zak transform based OTFS," *IEEE Commun. Lett.*, vol. 28, no. 3, pp. 672–676, Mar. 2024.

[20] S. P. Muppaneni, S. R. Mattu, and A. Chockalingam, "Channel and radar parameter estimation with fractional delay-Doppler using OTFS," *IEEE Commun. Lett.*, vol. 27, no. 5, pp. 1392–1396, May 2023.

[21] M. Marchese, H. Wymeersch, P. Spallaccini, and P. Savazzi, "Progressive inter-path interference cancellation algorithm for channel estimation using orthogonal time–frequency space," *Sensors*, vol. 24, no. 13, p. 4414, Jul. 2024.

[22] P. Raviteja, Y. Hong, E. Viterbo, and E. Biglieri, "Practical pulse-shaping waveforms for reduced-cyclic-prefix OTFS," *IEEE Trans. Veh. Technol.*, vol. 68, no. 1, pp. 957–961, Jan. 2019.

[23] Y. Wu, C. Han, and Z. Chen, "DFT-spread orthogonal time frequency space system with superimposed pilots for terahertz integrated sensing and communication," *IEEE Trans. Wireless Commun.*, vol. 22, no. 11, pp. 7361–7376, Nov. 2023.

[24] S. R. Mattu and A. Chockalingam, "Learning in time-frequency domain for fractional delay-Doppler channel estimation in OTFS," *IEEE Wireless Commun. Lett.*, vol. 13, no. 5, pp. 1245–1249, May 2024.

[25] S. R. Mattu and A. Chockalingam, "Learning based delay-Doppler channel estimation with interleaved pilots in OTFS," in *Proc. IEEE 96th Veh. Technol. Conf. (VTC-Fall)*, Sep. 2022, pp. 1–6.

[26] Y. Gao, X. Xu, B. Hu, J. Du, W. Yang, and Y. Jin, "Channel estimation for MIMO-OTFS satellite communication: A deep learning-based approach," in *Proc. 33rd Int. Conf. Comput. Commun. Netw. (ICCCN)*, Jul. 2024, pp. 1–6.

[27] L. Guo, P. Gu, J. Zou, G. Liu, and F. Shu, "DNN-based fractional Doppler channel estimation for OTFS modulation," *IEEE Trans. Veh. Technol.*, vol. 72, no. 11, pp. 15062–15067, Nov. 2023.

[28] X. Zhang, W. Yuan, C. Liu, F. Liu, and M. Wen, "Deep learning with a self-adaptive threshold for OTFS channel estimation," in *Proc. Int. Symp. Wireless Commun. Syst. (ISWCS)*, Oct. 2022, pp. 1–5.

[29] X. Zhang, W. Yuan, and C. Liu, "Deep residual learning for OTFS channel estimation with arbitrary noise," in *Proc. IEEE/CIC Int. Conf. Commun. China (ICCC Workshops)*, China, Aug. 2022, pp. 320–324.

[30] Q. Li, Y. Gong, F. Meng, Z. Li, L. Miao, and Z. Xu, "Residual learning based channel estimation for OTFS system," in *Proc. IEEE/CIC Int. Conf. Commun. China (ICCC Workshops)*, China, Aug. 2022, pp. 275–280.

[31] M. Marchese, H. Wymeersch, P. Spallaccini, S. Chinnici, and P. Savazzi, "Reduced-latency DL-based fractional channel estimation in OTFS receivers," in *Proc. IEEE Int. Conf. Mach. Learn. Commun. Netw. (ICMLCN)*, May 2025, pp. 1–6.

[32] G. Song, J. Bai, X. Wang, G. Wei, W. Yuan, and T. Q. S. Quek, "Low sidelobe level and PAPR OTFS waveform design for ISAC systems," *IEEE Trans. Commun.*, vol. 73, no. 9, pp. 7952–7966, Sep. 2025.

[33] P. Raviteja, K. T. Phan, Y. Hong, and E. Viterbo, "Orthogonal time frequency space (OTFS) modulation based radar system," in *Proc. IEEE Radar Conf. (RadarConf)*, Apr. 2019, pp. 1–6.

[34] M. F. Keskin, H. Wymeersch, and A. Alvarado, "Radar sensing with OTFS: Embracing ISI and ICI to surpass the ambiguity barrier," in *Proc. IEEE Int. Conf. Commun. Workshops (ICC Workshops)*, Jun. 2021, pp. 1–6.

[35] S. K. Dehkordi, L. Gaudio, M. Kobayashi, G. Colavolpe, and G. Caire, "Beam-space MIMO radar with OTFS modulation for integrated sensing and communications," in *Proc. IEEE Int. Conf. Commun. Workshops (ICC Workshops)*, May 2022, pp. 509–514.

[36] L. Gaudio, M. Kobayashi, G. Caire, and G. Colavolpe, "Joint radar target detection and parameter estimation with MIMO OTFS," in *Proc. IEEE Radar Conf. (RadarConf20)*, Sep. 2020, pp. 1–6.

[37] M. F. Keskin, C. Marcus, O. Eriksson, A. Alvarado, J. Widmer, and H. Wymeersch, "Integrated sensing and communications with MIMO-OTFS: ISI/ICI exploitation and delay-Doppler multiplexing," *IEEE Trans. Wireless Commun.*, vol. 23, no. 8, pp. 10229–10246, Aug. 2024.

[38] S. Singh, A. Nakkeeran, P. Singh, E. Sharma, and J. Bapat, "Target detection for OTFS-aided cell-free MIMO ISAC system," *IEEE Trans. Veh. Technol.*, vol. 74, no. 7, pp. 11568–11573, Jul. 2025.

[39] G. D. Surabhi and A. Chockalingam, "Low-complexity linear equalization for OTFS modulation," *IEEE Commun. Lett.*, vol. 24, no. 2, pp. 330–334, Feb. 2020.

[40] S. Tiwari, S. S. Das, and V. Rangamgari, "Low complexity LMMSE receiver for OTFS," *IEEE Commun. Lett.*, vol. 23, no. 12, pp. 2205–2209, Dec. 2019.

[41] A. Naikoti and A. Chockalingam, "Low-complexity delay-Doppler symbol DNN for OTFS signal detection," in *Proc. IEEE 93rd Veh. Technol. Conf. (VTC-Spring)*, Apr. 2021, pp. 1–6.

[42] A. Pfadler, P. Jung, T. Szollmann, and S. Stanczak, "Pulse-shaped OTFS over doubly-dispersive channels: One-tap vs. full LMMSE equalizers," in *Proc. IEEE Int. Conf. Commun. Workshops (ICC Workshops)*, Jun. 2021, pp. 1–6.

[43] P. Raviteja, K. T. Phan, Y. Hong, and E. Viterbo, "Interference cancellation and iterative detection for orthogonal time frequency space modulation," *IEEE Trans. Wireless Commun.*, vol. 17, no. 10, pp. 6501–6515, Oct. 2018.

[44] R. Chong, S. Li, Z. Wei, M. Matthaiou, D. W. K. Ng, and G. Caire, "Cross-domain iterative detection for OTFS transmission with frequency domain equalization," *IEEE Trans. Commun.*, vol. 73, no. 10, pp. 9886–9902, Oct. 2025.

[45] C. Byrne, "A unified treatment of some iterative algorithms in signal processing and image reconstruction," *Inverse Problems*, vol. 20, no. 1, pp. 103–120, Nov. 2003.

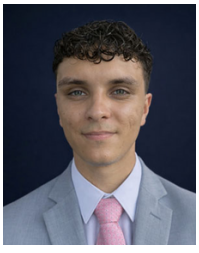
[46] H. K. I. Al-Mahdawi, H. Alkattan, M. Abotaleb, A. Kadi, and E.-S.-M. El-Kenawy, "Updating the Landweber iteration method for solving inverse problems," *Mathematics*, vol. 10, no. 15, p. 2798, Aug. 2022.

[47] Z. Wei, W. Yuan, S. Li, J. Yuan, and D. W. K. Ng, "Transmitter and receiver window designs for orthogonal time-frequency space modulation," *IEEE Trans. Commun.*, vol. 69, no. 4, pp. 2207–2223, Apr. 2021.

[48] M. A. Albreem et al., "Low complexity linear detectors for massive MIMO: A comparative study," *IEEE Access*, vol. 9, pp. 45740–45753, 2021.

[49] Z. Gong, F. Jiang, Y. Song, C. Li, and X. Tao, "Channel estimation, interpolation and extrapolation in doubly-dispersive channels," 2024, *arXiv:2408.09381*.

[50] S. R. Doha and A. Abdelhadi, "Deep learning in wireless communication receiver: A survey," 2025, *arXiv:2501.17184*.



MAURO MARCHESE (Graduate Student Member, IEEE) received the B.Sc. degree in electronic and computer engineering and the M.Sc. degree (summa cum laude) in electronic engineering from the University of Pavia, Italy, in 2022 and 2024, respectively, where he is currently pursuing the Ph.D. degree in electronics, computer science, and electrical engineering. His research interests include waveform and receiver design for 6G high-mobility communications, integrated sensing and communications (ISAC), and wireless sensor networks (WSNs). He was a recipient of the Leonardo Calandrino Degree Award from WiLab, National Inter-University Consortium for Telecommunications (CNIT), and the Ing. Carmelo Decanis Degree Award from the University of Pavia, in 2025, both awarded for his master's thesis.



MUSA FURKAN KESKIN (Senior Member, IEEE) received the Ph.D. degree in electrical and electronics engineering from Bilkent University, Ankara, Türkiye, in 2018. He is currently a Senior Researcher with the Department of Electrical Engineering, Chalmers University of Technology, Gothenburg, Sweden, with a specialization in integrated localization, communication, and sensing in 6G systems. His awards include the 2019 IEEE Türkiye Best Ph.D. Thesis Award for his work on visible light positioning systems, the EU MSCA Postdoctoral Fellowship for his project "OTFS-RADCOM: A New Waveform for Joint Radar and Communications Beyond 5G," and the Swedish Research Council (VR) Starting Grant for his project on "Localization and Sensing for Perceptive Cell-Free Networks Towards 6G." He has also served as the Winter School Chair for the IEEE JC&S Symposium 2026 and the TPC Co-Chair for VTC 2025 Spring and a member for EURASIP Technical Area Committee (TAC) Signal Processing for Communications and Networking (SPCN). He serves as an Associate Editor for IEEE TRANSACTIONS ON SIGNAL PROCESSING and IEEE TRANSACTIONS ON COMMUNICATIONS. Previously, he served as an Associate Editor for IEEE TRANSACTIONS ON MOBILE COMPUTING.



PIETRO SAVAZZI (Senior Member, IEEE) received the Laurea degree in electronics engineering and the Ph.D. degree in electronics and computer science from the University of Pavia, Italy, in 1995 and 1999, respectively. In 1999, he joined the Ericsson Laboratory Italy, Milan, as a System Designer, working on broadband microwave systems. In 2001, he was with Marconi Mobile, Genoa, Italy, as a System Designer in the field of 3G wireless systems. Since 2003, he has been with the University of Pavia, where he is currently an Associate Professor, teaching courses on signal processing and wireless communications and sensor networks. His main research interests are in signal processing and AI for wireless communication, sensor systems, and body-area and intra-body networks.



HENK WYMEERSCH (Fellow, IEEE) received the Ph.D. degree in electrical engineering/applied sciences from Ghent University, Belgium, in 2005. He is currently a Professor of communication systems with the Department of Electrical Engineering, Chalmers University of Technology, Sweden; and a Distinguished Visiting Professor with Tsinghua University. Prior to joining Chalmers, he was a Post-Doctoral Researcher with the Laboratory for Information and Decision Systems, Massachusetts Institute of Technology, from 2005 to 2009. His research interests include the convergence of communication and sensing, in a 5G and beyond 5G context. He served as an Associate Editor for IEEE COMMUNICATIONS LETTERS, IEEE TRANSACTIONS ON WIRELESS COMMUNICATIONS, and IEEE TRANSACTIONS ON COMMUNICATIONS. He is currently a Senior Member of IEEE Signal Processing Magazine Editorial Board. From 2019 to 2021, he was an IEEE Distinguished Lecturer with the Vehicular Technology Society.